Title

Collapse of late endosomal pH elicits a rapid Rab7 response via V-ATPase and RILP.

Running Title

LE response to pH collapse

Authors and Affiliations

Mulligan, R.J.[1,3,4], Magaj M.M.[2,3], Redemann S.[2,5], Yap C.C.[1], Winckler B[1].

[1]Department of Cell Biology, University of Virginia, Charlottesville, VA.
[2]Department of Molecular Physiology and Biological Physics, University of Virginia, Charlottesville VA.
[3]Cell and Developmental Biology Graduate Program, University of Virginia, Charlottesville, VA.
[4]Medical Scientist Training Program, University of Virginia, Charlottesville, VA.
[5]Center for Membrane and Cell Physiology, University of Virginia, Charlottesville, VA.

Summary

Using a lysosomal damage model, Mulligan et al. demonstrates that pH collapse in otherwise undamaged late endosomes leads to V-ATPase- and RILP-mediated hyperactivation of the small GTPase Rab7, disrupting normal late endosome tubulation behavior and biosynthetic receptor trafficking. These findings suggest a pH driven late endosomal stress response.

Abstract

Endosomal-lysosomal trafficking entails progressive acidification of endosomal compartments by the H^+-V-ATPase to reach low lysosomal pH. Disruption of proper pH affects lysosomal function and the balance of protein synthesis and degradation (proteostasis). Disruption of endosomal pH also impairs endocytic maturation upstream of the lysosome. Using a lysosomal damage model (LLOMe), we identify the late endosomal small GTPase Rab7 as a rapid responder to endosomal/lysosomal pH neutralization. Luminal pH neutralization in LLOMe leads to increased assembly of the V_1G_1 subunit of the V-ATPase on endosomal membranes and stabilization of Rab7 in the GTP-bound form. Rab7 stabilization is driven by a combination of pump assembly and the Rab7 effector RILP, while contributing to loss of late endosome tubulation and recycling of membrane receptors, like CI-M6PR. Our findings suggest a physiological cascade on late endosomes driven by V-ATPase assembly and Rab7 stabilization to counteract pH neutralization, and a novel model of how late endosomes broadly contribute to cellular stress responses, including LLOMe-mediated damage.

Introduction

Lysosomes are the principal membrane-bounded proteolytic compartment within cells and are the endpoints of degradative endocytic trafficking, phagocytosis and autophagy. Progression of these pathways to lysosomes is essential for maintaining the balance of protein synthesis and degradation within the cell (i.e., proteostasis). Before reaching lysosomes, endocytosed cargo destined for degradation traffics through a series of endosomal compartments, including early

(sorting) endosomes (EE), late endosomes (LE) and ultimately lysosomes (LYS). Trafficking is achieved through fission and fusion of vesicular carriers and progressive compartmental maturation culminating in the highly acidic and degradative lysosome. LEs specifically represent a crossroads where endocytosed cargos encounter increasingly activated lysosomal hydrolases in increasingly acidified compartments before fusing with mature, maximally degradative LYS.

LE maturation is triggered by switching of Rab family proteins (i.e., Rab5 to Rab7), from which active GTP-bound Rab7a (herein, Rab7) can engage effector proteins. Some of the better studied Rab7 effectors include the core retromer complex (Vps26/29/35) and RILP. Retromer has been implicated in some cell types in retrieval of trafficking receptors like mannose-6-phosphate receptors (M6PRs) from LEs back to the trans-Golgi network (TGN), and for the generation of membranous tubules necessary for recycling events. RILP links LEs to dynein motors for motility. RILP/Rab7 complexes are also involved in tubule formation from LYS in some cell types (Mrakovic et al., 2012). These tubules require proper GTP cycling for their formation (Markworth et al., 2021). Our knowledge of Rab7 containing tubules is still limited beyond this.

Maturation of LEs involves decreasing intra-endosomal pH to that of the highly acidic lysosome (pH≈4.5). Correct endosomal/lysosomal pH is critical for lysosomal degradation, ligand-receptor dissociation events (e.g., cathepsin release from M6PRs), regulating vesicular fusion events, vesicle motility, and organellar positioning (Chadwick et al., 2021; Freeman et al., 2023). However, the mechanisms by which luminal pH can coordinate cytoplasmic effectors, like Rabs, is not well understood. Normally, cells establish and maintain endo/lysosomal pH through the activity of the endosome/lysosome localized vacuolar H^+-ATPase (V-ATPase), which is regulated by the assembly of the cytosolic V_1 complex with the membrane embedded V_0 domain (Collins and Forgac, 2020). Rab7 has been implicated in V-ATPase function and endosomal acidification by forming a ternary complex with RILP and the V_1G_1 subunit of the V_1-ATPase complex (De Luca et al., 2014) and through direct interaction with the V_0a_3 subunit in secretory lysosome trafficking in osteoclasts (Nakanishi-Matsui and Matsumoto, 2022). However, the precise connections between Rab7, endosomal acidification, and V_0-V_1 assembly are not yet well elucidated.

Not surprisingly, numerous pathologies associated with impaired degradation or membrane trafficking to lysosomes have been identified and is thus a topic of intense research. For instance, it has become clear that LYS can be directly damaged by a variety of cellular insults leading to a process of lysosomal membrane permeabilization (LMP) (or lysosomal membrane damage, herein used interchangeably). LMP is defined as any perturbation of the lysosomal limiting membrane that compromises membrane integrity and leads to leakage of luminal lysosomal content into the cytosol (Wang et al., 2018). This includes leakage of protons (pH neutralization), loss of certain proteins like cathepsins, and loss of other ionic stores, like calcium, zinc, and iron (Lakpa et al., 2021). LMP contributes to the pathology of numerous diseases, including lysosomal storage disorders (Kirkegaard et al., 2010) and those with neurotoxic aggregates (Freeman et al., 2013; Flavin et al., 2017; Polanco and Götz, 2021; Dilsizoglu Senol et al., 2021) (collectively referred to as sterile insults), as well as during infections with many pathogens (regarded as non-sterile insults). It is thus of great importance to elucidate how cells respond to LMP.

Our understanding of cellular LMP responses has been greatly advanced through use of the small dipeptide L-leucyl L-leucine-O-methyl-ester (LLOMe). LLOMe is a lysosomotropic weak base. At neutral pH, it freely dissociates across cell and organelle membranes but upon encountering highly acidic environments, like that of the lysosome, it becomes trapped, and exhibits membrane-lytic properties. Studies into how cells respond to LMP using LLOMe as a model have elucidated two key pathways. First, milder LMP (small membrane disruption) initiates mechanisms that directly repair the damaged lysosomal membrane within minutes. Together, endosomal sorting complex required for transport (ESCRT) (Skowyra et al., 2018; Radulovic et al., 2018; Jia et al., 2020a; Bohannon and Hanson, 2020), annexins A1/A2 (Yim et al., 2022), sphingomyelin scramblases (Niekamp et al., 2022), and phosphatidyl-inositol-4-phosphate (PI4P)

production (Tan and Finkel, 2022; Radulovic et al., 2022) facilitate direct membrane repair. These repair mechanisms have all been shown to be dependent on local Ca^{2+} release from damaged lysosomes. Secondly, extensive LMP (large, widespread membrane disruption) can no longer be repaired, and damaged lysosomes are cleared through lysosome-specific autophagy, or lysophagy, within hours (Papadopoulos et al., 2020; Jia et al., 2020b; Zoncu and Perera, 2022; Yang and Tan, 2023). Canonically, extensive LMP is indicated by the binding of the cytosolic lectin galectin-3 (Gal3) to the inner glycocalyx on the lysosomal membrane inner leaflet. Beyond the two key pathways of repair and lysophagy, recent studies have also discovered a role for recycling of lysosomal membrane proteins (Eriksson et al., 2020) and membrane tubulation from damaged lysosomes to generate new lysosomes *de novo*. At long time points following LLOMe exposure (>2 hours), the microtubule adaptor JIP4 on damaged lysosomes aids in generating LAMP1 (lysosomal associated membrane protein 1) negative tubules (Bonet-Ponce et al., 2020). Interestingly, active Rab7 negatively impacts tubulation from damaged lysosomes as loss of the GTPase activating protein (GAP) TBC1D15 severely impacts tubule formation (Bhattacharya et al., 2023).

Notably, studies on both membrane repair and lysophagy after LMP have largely focused on the molecular events at the level of the lysosomal membrane itself after extensive damage. To what degree other kinds of endosomes necessary for proper membrane trafficking contribute to cellular stress responses to LMP is not known. Specifically, it is not known if LEs, which are themselves moderately acidic, are also damaged and mount a cellular stress response. LEs and LYS are often combined in the literature into one category of “endosome/lysosomes”, but they are distinct organelles and may serve different purposes in LMP. Finally, there is limited exploration of a mechanistic role for pH neutralization in sterile LMP contexts. It is not known how regulated assembly of the V-ATPase also occurs in the context of sterile LLOMe-elicited LMP, and what downstream effects this might have. We thus investigated if and how LEs contribute to LMP responses by focusing on the principal LE Rab, Rab7, and its connection to pH neutralization. We find that bona fide Rab7-LEs (as opposed to LYS) respond to pH neutralization, irrespective of membrane damage. In response to LLOMe-mediated endosomal/lysosomal pH neutralization, the V-ATPase subunit V_1G_1 increasingly assembles on endosomal membranes and increases Rab7 membrane stabilization. In addition to V-ATPase assembly, the Rab7 effector RILP contributes to the increased membrane stability of Rab7. Finally, we report changes in Rab7 tubulation and in biosynthetic trafficking of M6PRs when pH collapses in late endosomes, leading to the novel idea that LEs are rapid responders to pH collapse via a V-ATPase-Rab7 axis.

Results

LLOMe disrupts lysosomes in NRK cells leading to expected LMP responses

We sought to ask whether endosomal organelles upstream of LYS were impacted in LMP. To do so, we used LLOMe to pharmacologically induce LMP in normal rat kidney cells (NRK) and mouse embryonic fibroblasts (MEFs). We first tested if these cells responded to LLOMe as previously described for other cell lines. We focused on key LMP responses including pH neutralization of lysosomes, direct membrane repair processes (i.e., ESCRT), and lysophagy (i.e., Gal3). In order to monitor pH neutralization, we loaded pH-sensitive FITC dextran and pH-insensitive TMR-dextran together into lysosomes overnight before LLOMe treatment. We used dextran sizes previously demonstrated to be retained within damaged lysosomes following LLOMe treatment (Repnik et al., 2017). FITC-dextran de-quenched rapidly (within 4 minutes) after LLOMe administration, indicative of lysosomal pH neutralization (Fig. 1 A-C, Video 1). To observe the kinetics of minimal LMP events, we then acutely loaded cells with the substrate Magic-Red Cathepsin B (MR-B), which is a small peptide that fluoresces when proteolytically cleaved by cathepsin B in degradative lysosomes. As opposed to the larger dextrans, the small fluorescent

product of MR-B proteolysis is lost from degradative compartments within 1 minute of LLOMe administration, indicating the presence of minimal LMP and leakage into the cytosol (Fig.S1 A-C, NRKs). We next monitored repair machinery by staining endogenous ESCRT components (ALIX). Since the ALIX antibody did not work on rat cells, we carried out these experiments in MEFs. We observed rapid increase in ALIX staining after 5 minutes of LLOMe addition, indicative of ESCRT membrane repair after minimal LMP (Fig. 1 D-E, MEFs). Finally, endogenous galectin-3 (Gal3) was increasingly recruited into distinct puncta over time, indicative of extensive LMP and lysophagy (Fig. 1 F-G).

Having established that LLOMe drives LMP as expected in our system, we then used a multi-marker immunostaining approach to ask whether LLOMe affects organelles upstream of lysosomes, starting with Golgi and early endosomal organization. LLOMe treatment did not disrupt Golgi stacks, as localization of markers for both the cis-Golgi (GM130) and trans-Golgi network (TGN38) were not altered (Fig. S2 A). The early endosomal (EE) marker EEA1 was also not altered following LLOMe treatment, suggesting early endosomes were normal (Fig. S2 B). In contrast, we observed marked changes in Rab7 staining, a canonical late endosomal protein, after 1 hour of LLOMe treatment (Fig. 1 H), as compared to vehicle (DMSO) controls. Staining was often punctate and seemed to decorate the edge of an enlarged compartment. The apparent volume of individual Rab7 compartments was increased whereas conversely the total number was decreased in LLOMe (Fig. 1 I-J). Because Rab7 immunostaining on apparent enlarged structures was discontinuous and cage-like, we wondered whether these were single compartments or clustering of smaller vesicles. To distinguish between these possibilities, we performed ultrastructural analysis using thin-section transmission electron microscopy (TEM). TEM revealed the presence of numerous enlarged single-membraned vacuolar-like structures in LLOMe rather than clusters of small vesicles (Fig. 1 K), confirming our interpretation of the immunostaining as enlarged Rab7+ compartments. Notably, some of these structures have observable material within the lumen (black arrowhead) whereas others are highly lucent (yellow arrowhead), suggesting that not all of the enlarged compartments are lysosomes. Together, these results show that Rab7+ compartments respond to LLOMe-induced lysosomal damage.

Late endosomes rapidly respond to LLOMe.

Lysosomal responses to LMP have been extensively described. Given that Rab7 is present on multiple endosomal compartments, including transitioning early to late endosomes (EE-LE), late endosomes (LEs), and lysosomes (LYS), we wondered whether the responding Rab7+ compartments corresponded only to LYS or included LEs and transitioning EE-LEs. A response in upstream endosomal compartments to downstream lysosomal damage would be notable in suggesting the endosomal system as a whole responds to damage of terminal compartments. We have previously distinguished EEs, LEs and LYS on the basis of multi-marker immunostaining and degradative capacity (Yap et al., 2018). We define these compartments for use in this work as follows: EEs are EEA1-positive but low in Rab7 (EE=EEA1+, Rab7*lo*). LEs are Rab7-positive, but not highly degradative compartments and thus low in degradative enzymes, such as cathepsin-B (CatB). Given their low degradative capacity, LEs also show only low staining with the degradative sensor DQ-BSA, which turns red in degradative compartments (LE=Rab7+, CatB/DQ-BSA*lo*). LYS are usually Rab7-positive and highly degradative. They are therefore positive for CatB and DQ-BSA turns red (LYS=Rab7+, CatB/DQ-BSA*hi*) (Fig. 2 A). As compared to controls, EEs (EEA1+, Rab7*lo*) in LLOMe treated cells were not disrupted nor was the colocalization of Rab7 and EEA1 signal (Fig. S2 B-D). Interestingly, however, both LEs (Rab7+CatB*lo*: empty arrowhead) and LYS (Rab7+CatB*hi:* yellow filled arrowhead) were altered following LLOMe treatment (Fig. 2 B). Both CatB and LAMP1 (lysosomal associated membrane protein 1) staining was only mildly (LAMP1) or not enriched (CatB) on Rab7 endo-lysosomes following LLOMe treatment (Fig. 2 C-D). These data suggest that LLOMe-mediated LMP leads to

phenotypic alterations in both Rab7+ LEs and LYS but not transitioning EE-LEs. To further confirm this, and in order to determine the kinetics of Rab7+ LE responses to LLOMe, we carried out live imaging of NRK cells stably expressing Emerald-Rab7 and loaded overnight with the degradative sensor DQ-BSA prior to LLOMe treatment to distinguish highly degradative Rab7+ lysosomes from lowly degradative LEs. We observed rapid increases in apparent area of both LEs (Rab7+DQ*lo)* and LYS (Rab7+DQ*hi)* in the first 10 minutes following LLOMe exposure (Fig. 2 E-I, Fig. S2 E, Video 2).These compartments continued to increase in size over time. Together, these data show that Rab7+ LEs are novel rapid responders to LLOMe-mediated cellular damage and might thus contribute to cellular responses to LMP.

LLOMe does not rupture Rab7-positive late endosomes but does neutralize their pH

Given the lysosomotropic and weak base properties of LLOMe, more LLOMe will concentrate in more acidic, mature compartments (i.e., LYS) compared to earlier more neutral compartments (i.e., EEs) (Thiele and Lipsky, 1990; Uchimoto et al., 1999). Since LEs are relatively acidic (~pH 5.5), we hypothesized that Rab7+ LEs concentrate enough LLOMe to damage their membranes. The similarities between Rab7+ LEs and LYS following LMP would then be due to membrane damage of both types of compartments. Alternatively, it is possible that LLOMe only damages membranes of highly acidified LYS. In this case, two possible alternative hypotheses are that Rab7+ LEs are responding at a distance to the leaking luminal content (e.g., Ca^{2+}) from damaged LYS or that Rab7+ LEs are undergoing a direct LLOMe-mediated stress response in the absence of membrane damage.

To evaluate these hypotheses, we first determined if LEs are themselves damaged. We stained for endogenous ALIX (as in Fig. 1) combined with Rab7 and partitioned LEs from LYS by CatB intensity. Following 5 minutes of 1mM LLOMe exposure, ALIX was markedly recruited to organelles as compared to controls (Fig. 3 A-B; yellow). We observe both damaged (ALIX+) and undamaged (ALIX-) LYS (Rab7+CatB*hi*) and LEs (Rab7+CatB*lo*) (Fig. 3 C). Quantification of damaged species revealed >50% of LYS recruited ALIX within the first 5 minutes of LLOMe exposure (Fig. 3 D) while only ~15% of LEs did (Fig. 3 E). Of the total LLOMe induced ALIX+ compartments, 67.82% were LYS while only 32.18% are LEs (Fig. 3 F). Thus, these data suggest that LYS are the predominant species with membrane damage following LLOMe, while LE membranes are largely preserved. To see if Rab7+ endosomes would progress to stages of extensive LMP that could initiate lysophagy, we co-immunostained treated NRK cells for Rab7 and Gal3 after 1 hour of LLOMe exposure. We observed minimal overlap of Rab7 compartments with Gal3 at later time points, indicating the majority of LEs do not develop extensive damage (Fig. 3 G).

Since the majority of LEs did not show membrane damage after LLOMe, we next investigated the alternative hypothesis that leaking luminal content from damaged LYS might cause phenotypic changes in size and number of Rab7 LEs in response to LMP. In particular, local Ca^{2+} release from LYS after LLOMe is required for both ESCRT-dependent and -independent repair mechanisms (Skowyra et al., 2018; Yim et al., 2022; Niekamp et al., 2022; Tan and Finkel, 2022; Radulovic et al., 2022). Cytosolic Ca^{2+} release can also elicit signaling through adaptor proteins (Clapham, 2007) that have profound impacts on membrane trafficking (Chadwick et al., 2021), and thus might be the communicable signal for phenotypic changes to Rab7+ LE size and number. Thus, we modulated LYS Ca^{2+} release in two ways (Fig. S3 A). First, we chelated local Ca^{2+} release from damaged LYS using cells pre-treated with cell-permeable BAPTA-AM prior to LLOMe exposure. BAPTA-AM did not prevent observable LLOMe-mediated changes in Rab7 compartment size, even though Ca^{2+}-dependent ALIX recruitment was inhibited (Fig. S3 B-D). Conversely, we stimulated LYS Ca^{2+} release in the absence of LMP using ML-SA1, an agonist of the Ca^{2+}-permeable channel TRPML1, to drive Ca^{2+} ions from the lysosomal lumen into the cytosol. Live imaging of NRK cells expressing Em-Rab7^{WT} and treated with ML-SA1 revealed Ca^{2+} release alone was not sufficient to cause the changes in Em-

Rab7^{WT}distribution observed for LLOMe (Fig. S3 E, Video 3). As amino acid flux and nutrient availability are increasingly reported as a signaling mechanisms for lysosomal behavior, we also broadly tested if disruption of protein degradation, and thus inhibition of amino acid flux, would prevent changes in Rab7+ LE size and number. To do so, we loaded Em-Rab^{WT} expressing NRK cells with the degradative sensor DQ-BSA and pre-treated cells with the pan-cathepsin inhibitor E-64D for 2 hours prior to LLOMe exposure. Live imaging revealed that lysosomal degradation was inhibited, as indicated by lack of DQ-BSA signal. E-64D caused perinuclear clustering of Rab7+ compartments but did not prevent changes to Rab7+ compartment size or intensity (Fig. S3 F). Together, these data suggest that local LYS signals that emanate from damaged LYS during LMP, including Ca^{2+} release and amino acids, are not responsible for observable changes in Rab7+ LEs.

Finally, we investigated the hypothesis that Rab7+ LEs were undergoing a direct LLOMe-mediated stress independent of membrane damage. Again, given the weak base properties of LLOMe, we posited that LLOMe treatment might lead to direct pH neutralization of LEs, irrespective of ALIX+ membrane damage. To test this, we loaded cells with the degradative sensor DQ-BSA overnight (to mark LYS), and then acutely loaded pH-sensitive Oregon Green dextran for 1 hour (to populate all endocytic compartments), before live imaging of cells exposed to vehicle (DMSO) or LLOMe (Fig. 4 A). As expected, LLOMe treatment led to rapid de-quenching of Oregon-Green dextran in LYS (DQ*hi)*, indicative of pH neutralization (Fig. 4 B-D, yellow arrowhead, Video 4). Similarly, the pH of LEs (DQ*lo)* was also neutralized following LLOMe treatment (Fig. 4 B, E-F, empty arrowhead, Video 4). Overall, these data suggest that while LLOMe does not extensively damage LEs as compared to LYS, it is sufficient to neutralize their pH, concomitant with changes in size and number of Rab7 compartments.

pH gradient collapse is sufficient to phenocopy many LLOMe-driven Rab7 phenotypes

Since LLOMe neutralizes the luminal pH of both LE and LYS (Fig. 1A-C, Fig. 4), we next wondered whether pH collapse alone is sufficient to lead to the observed changes in Rab7. To do so, we perturbed endosomal/lysosomal pH pharmacologically in two ways followed by fixed immunostaining and quantification of Rab7+ endosome/lysosomes changes (Fig. 5 A). We first used treatments with NH_4Cl to neutralize luminal pH (Fig. 5 B). As a weak base, NH_4Cl freely diffuses across membranes and becomes protonated and concentrates in acidic compartments. Treatment of cells with 20mM NH_4Cl for 1 hour resulted in enlarged Rab7+ endosome/lysosomes, but the effect was smaller than for LLOMe (Fig. 5 C). However, quantification revealed that the total number of Rab7+ endosome/lysosomes was comparably reduced in NH_4Cl and LLOMe (Fig. 5 D). Rab7 staining on endosome/lysosomes was increased in both conditions, although the p-value for NH_4Cl did not reach statistical significance (Fig. 5 E). As a whole, Rab7 endosome/lysosome responses to NH_4Cl were less pronounced than those to LLOMe. We also disrupted endosomal/lysosomal pH by directly inhibiting the V-ATPase, using Bafilomycin-A1 (BafA1). BafA1 blocks key interactions within the V-ATPase V_0 domain, thereby preventing proton translocation and rotary domain rotation (Wang et al., 2021). Importantly, we used treatment times and concentrations of BafA1 that were previously shown to have primary effects on endosomal/lysosomal acidification but not secondary effects on endo-lysosome fusion (Klionsky et al., 2008). Rab7+ endosomes/lysosomes in cells treated with 200nM of BafA1 for 2 hours increased in size, reduced in number, and increased in Rab7 intensity as compared to controls (Fig. 5 F-I). Similar to NH_4Cl, these responses were milder and qualitatively more heterogeneous compared to LLOMe. To determine if these pH disruptive treatments caused LMP, we screened for the canonical early (ALIX) and late (Gal3) LMP response markers in NH_4Cl and BafA1 treated cells by fixed immunostaining. Importantly, only LLOMe treatment led to accumulation of ALIX and Gal3 (Fig. 5 J). Together these data suggest that pH neutralization alone (i.e., NH_4Cl and BafA1) is sufficient to alter Rab7+ endosome/lysosome intensity, area and number, but not sufficient to trigger membrane damage.

LLOMe-mediated pH collapse recruits V-ATPase V_1 subunits to late endosomes and lysosomes independently of Rab7

We have shown that luminal pH neutralization is sufficient to lead to many of the changes in Rab7+ endosome/lysosomes seen in LLOMe, including increased Rab7 intensity on the endosomal surface. We next asked how pH changes in the endosomal lumen might be sensed by cytosolic Rab7. V_0 subunits have been previously shown to be responsive to luminal pH changes (Hurtado-Lorenzo et al., 2006; Marshansky, 2007), making the V-ATPase itself a likely candidate to transmit information across the endosomal membrane. Further, in yeast and HEK293T cells, vacuolar and lysosomal pH neutralization, respectively, leads to increased pump assembly (Shao and Forgac, 2004; Stransky and Forgac, 2015). We thus hypothesized that LLOMe-mediated pH neutralization would lead to increased V-ATPase assembly (and thus activity) in order to homeostatically reestablish low luminal pH. To test this, we overexpressed an HA-tagged version of V_1G_1 in COS-7 cells and co-immunostained for endogenous Rab7 and the HA-tag. 30 minutes of 1mM LLOMe treatment led to increased V_1G_1 on Rab7 endosomes as compared to controls, consistent with increased V-ATPase assembly (Fig. 6 A-B). We note that in COS-7 cells, as compared to previous experiments with NRK and MEFs, the total number of endogenous Rab7 compartments is decreased at baseline, however, there are still changes in Rab7 phenotype (i.e., endosome size and Rab7 intensity) consistent with earlier observations. To then test whether V_1G_1 recruitment occurred to LEs or LYS, we loaded HA-V_1G_1 transfected COS-7 cells with DQ-BSA overnight to mark LYS. After LLOMe treatment, we observed increased recruitment of HA-V_1G_1 to both LEs (DQ*lo)* and LYS (DQ*hi)* Rab7+ compartments (Fig. 6 C). These data suggest that LLOMe-induced pH neutralization increased pump assembly on both LEs and LYS. Given that LEs themselves are not extensively damaged (Fig. 3), these data also suggest that membrane damage is not a pre-requisite for V-ATPase assembly in LMP.

Rab7 indirectly associates with the V-ATPase via a ternary Rab7-RILP-V_1G_1 complex, where RILP is an intermediate partner between Rab7 and V_1G_1 (De Luca et al., 2014). Since both Rab7 and V_1G_1 levels are increased on endo-lysosomes following LLOMe, we hypothesized that Rab7 activity might control V_1G_1 localization and thus V-ATPase activity following pH neutralization. To investigate this hypothesis, we overexpressed either GFP-tagged wild-type (WT) Rab7, constitutively active (CA, Q67L) Rab7, or dominant negative (DN, T22N) Rab7 with HA-V_1G_1 in COS-7 cells and then tested LLOMe treatment (Fig. S4 A-C). If Rab7 is responsible for HA-V_1G_1 assembly on endosomal membranes, we expected CA-Rab7^{Q67L} to drive HA-V_1G_1 assembly regardless of LLOMe treatment, and DN-Rab7^{T22N} to prevent HA-V_1G_1 assembly in LLOMe. Surprisingly, we found no increase in HA-V_1G_1 assembly with CA-Rab7^{Q67L} expression alone, even though Rab7 is highly recruited and endosomes were greatly enlarged (Fig. S4 B, D-E). Similarly, HA-V_1G_1 assembly in LLOMe was not inhibited by DN-Rab7^{T22N} (Fig. S4 C-E), but interestingly, DN-Rab7^{T22N} was increasingly recruited to HA-V_1G_1 compartments. This begins to suggest a possible nucleotide-independent mechanism for the initial Rab7 recruitment in LLOMe. To test whether Rab7 was required at all for HA-V_1G_1 localization, we isolated primary MEFs from Rab7$^{fl/fl}$ mice and transiently transfected them with Cre-GFP and HA-V_1G_1. Despite the lack of Rab7 in Cre-GFP+ cells, HA-V_1G_1 localized normally to endosomes under untreated conditions. (Fig. S4 F). Together, these data suggest that LLOMe leads to proton pump assembly (V_1G_1 recruitment) on both LEs and LYS independently of Rab7.

V-ATPase assembly contributes to Rab7 membrane stabilization

Since Rab7 was not required for V_1G_1 recruitment we tested if the initial V-ATPase assembly in response to pH neutralization instead influences Rab7 behavior. To test this hypothesis, we first determined whether pH neutralization alone was sufficient to recruit HA-V_1G_1 to endosomes. We overexpressed HA-V_1G_1 in COS-7 cells and subsequently treated them with

either DMSO, 1mM LLOMe, 20mM NH_4Cl, or 200nM BafA1. Whereas LLOMe and NH_4Cl treatment led to high degrees of recruitment of HA-V_1G_1 to endosomal compartments, BafA1 did not (Fig. 6 D-F). Though not proven, the lack of increased proton pump assembly in BafA1 suggests that rotary function of the V_0 domain might be involved in pH sensing mechanisms. This is consistent with recent data that BafA1 does not lead to increased V-ATPase assembly, despite an acidification defect (Hooper et al., 2022). Therefore, LLOMe and NH_4Cl lead to pH neutralization with pump assembly (i.e., V1G1 recruitment) whereas BafA1 leads to pH neutralization without pump assembly.

We next asked if Rab7 dynamics were changed as a result of proton pump assembly. Previous work reported slowed exchange of CA-Rab7^{Q67L} on endosomes using fluorescence recovery after photobleaching (FRAP) (McCray et al., 2010). Thus, to test membrane stability and exchange rates of Rab7, we carried out FRAP on Rab7+ endosome/lysosomes in stably expressing Em-Rab7^{WT} NRK cells under various pH neutralizing conditions (Fig. 7 A, Video 5). Control FRAP experiments led to 50% recovery of Rab7 fluorescence within 1 minute after bleaching and complete recovery to pre-bleach intensity within 4 minutes (Fig. 7 A-C, black). On the contrary, LLOMe treatment led to slower (Fig. 7 A-B, pink) and incomplete fluorescence recovery, which was significantly different than that of controls (Fig. 7 C, pink). This suggests that Rab7 is hyper-stabilized on enlarged endosome/lysosomes in LLOMe. Rab7 fluorescence recovery in NH_4Cl-treated cells was also significantly slower than controls, but recovered slightly faster than in LLOMe (Fig. 7 A-B, teal). However, plateau intensities were not significantly different from that of LLOMe (Fig. 7 C, teal). Interestingly, while BafA1-treated Rab7 endosome/lysosomes also recovered significantly slower than controls, they recovered significantly faster compared to LLOMe (Fig. 7 A-B, dark purple) and to a significantly greater plateau value (Fig. 7 C, purple), indicating lower degrees of membrane stabilization. Single exponential phase fitting of FRAP curves (Fig. 7 G) confirmed these findings and revealed altered half-times of recovery following pH neutralizing conditions, as compared to controls. Specifically, while the half time in control cells was very quick ($t_{1/2}$= 54.87s), LLOMe greatly extended this ($t_{1/2}$= 188.2s), whereas BafA1 treatment only partially impacted recovery rate ($t_{1/2}$= 66.1s). Putting these data together, pH neutralization conditions that enhanced V-ATPase assembly (i.e., LLOMe and NH_4Cl) stabilized Em-Rab7 association with LE/LYS membranes, whereas conditions without V-ATPase assembly (i.e., BafA1) did so to a significantly lesser degree (Fig. 7 H).

We further investigated Rab7 stabilization on endo/lysosomal membranes in response to LLOMe by asking if an intact Rab7-RILP-V_1G_1 complex was required. To do so, we created a stable NRK line overexpressing mutant Em-Rab7^{L8A} at comparable levels to stable Em-Rab7^{WT} cells, which cannot bind RILP (Wu et al., 2005) and thus lacks V_1G_1 binding. Given Rab7 is non-essential for HA-V_1G_1 responses to LLOMe (Fig. S4), V-ATPase assembly is intact under these conditions. We then subjected these cells to similar FRAP experiments as wild-type. In control conditions, Em-Rab7^{L8A} recovered similarly to Em-Rab7^{WT} following photobleaching (Fig. 7 D-E, light purple). However, in LLOMe conditions, recovery of Em-Rab7^{L8A} on endosome/lysosomes was faster than that of Em-Rab7^{WT} treated with LLOMe (Fig. 7 D-E, blue). While plateau values of control Em-Rab7^{L8A} were not significantly different from control Em-Rab7^{WT} conditions, LLOMe-treated Em-Rab7^{L8A} recovered to a significantly greater degree than LLOMe-treated Em-Rab7^{WT} cells (Fig. 7 F). Single exponential fitting of FRAP curves (Fig. 7 G) further revealed differences between Em-Rab7^{WT} and Em-Rab7^{L8A} cells. Specifically, the half time in control treated Em-Rab7^{L8A} cells was strikingly fast as compared to control treated Em-Rab7^{WT} ($t_{1/2}$=34.10s vs. 54.87s). Fitting also confirmed the half time in Em-Rab7^{L8A} cells treated with LLOMe was much shorter than the equivalent treatment in Em-Rab7^{WT} cells ($t_{1/2}$= 90.84s vs. 188.2s). Interestingly, the fitted recovery of Em-Rab7^{L8A} in LLOMe closely resembled that of BafA1 treatment (Fig. 7 G). These data together suggest that Rab7 is less stabilized on membranes following LLOMe in the absence of RILP binding (Fig. 7 H). Notably, Em-Rab7^{L8A} compartments were still vacuolar and still recruited additional Rab7, suggesting that these other Rab7 phenotypes occur independently

of RILP and may explain the partial nature of Em-Rab7^{L8A} recovery. Since both BafA1 and Em-Rab7^{L8A} conditions independently led to partial rescue of Em-Rab7 recovery relative to LLOMe, we suggest that both V-ATPase assembly and RILP contribute to Rab7 membrane stability.

Constitutively active (CA) Rab7^{Q67L} overexpression leads to accumulation of activated Rab7 on enlarged endosomes (Bucci et al., 2000) (Fig. S4 B). As well, LLOMe treatment leads to increased Rab7 intensity on enlarged endosomes and increased membrane stability by FRAP, which together strongly suggest increased levels of GTP-bound Rab7. Thus, we sought to test whether LLOMe alters Rab7 nucleotide binding status. We co-expressed GFP-tagged Rab7^{WT} or CA-Rab7^{Q67L} with a GST-fusion protein containing the Rab7-binding domain of RILP, to specifically capture active Rab7-GTP. This assay revealed a moderate but consistent increase (20%) in GTP-Rab7 in LLOMe, as compared to vehicle controls (Fig. 7 I-J). The degree of GTP binding in LLOMe was less than the CA-Rab7^{Q67L} positive control, which provided the level of maximal possible GTP binding. Altogether, these data reveal that LLOMe-mediated LMP leads to hyper-activation of Rab7 and stabilization on endosomal/lysosomal membranes in a manner partially influenced by V-ATPase assembly and RILP binding.

Hyperactivation of Rab7 leads to deficits in Rab7 effector-driven tubulation and receptor trafficking

Last, we sought to investigate if upstream membrane trafficking was disturbed by LLOMe-mediated pH neutralization and Rab7 hyperactivation. Many receptors are retrieved from LEs in tubules prior to fusion with lysosomes, including cation-independent mannose-6-phosphate receptor (CI-M6PR), which is retrieved from LEs back to the TGN. Recent findings suggest that Rab7 needs to be inactivated for some tubulation events to take place (Bhattacharya et al., 2023). These findings, in concert with ours demonstrating Rab7 hyperactivation and deregulated late endosomal behavior, led us to first investigate whether tubulation behavior of Rab7-labeled-LEs was impacted in acute timeframes following LLOMe treatment. We used primary MEFs transfected with Em-Rab7^{WT} and loaded continuously with tetramethyl-rhodamine dextran (TMRdex) cargo for 2 hours without a chase period to populate all levels of the endocytic pathway, before treating with either DMSO or 1mM LLOMe for 30 minutes. Live imaging of Em-Rab7+TMRdex+ compartments in DMSO revealed a relative abundance of tubules emanating from Rab7+ compartments (Fig. 8 A). Interestingly, the exposure to LLOMe led to a significant reduction in the number of Em-Rab7^{WT}+ dextran-containing tubules per cell as compared to controls (Fig. 8 A-B). The small number of tubules still forming in LLOMe treated conditions were shorter than controls, and had a reduced range of sizes (Fig. 8 C). To characterize acute tubule dynamics and in relation to pH neutralization following LLOMe, we performed live imaging of cells loaded with DQ-BSA and FITC dextran. Degradative DQ-BSA containing (LYS) tubules collapsed within 2 minutes of LLOMe exposure, which was temporally linked to the de-quenching of FITC dextran (i.e., increased luminal pH) within the tubule (Fig. 8 D, Video 6). Together, these data suggest that Rab7+ tubules, which appear to contain luminal cargo, are greatly reduced in the presence of LLOMe-mediated pH neutralization.

Lastly, we hypothesized that tubulation loss in LLOMe would contribute to mis-sorting of specific Rab7-dependent cargoes known to be sorted and recycled via endosomal tubules. It has long been established that pH neutralization within endosomes impacts the recycling of trafficking receptors (plasmalemmal or endosomal) back to the Golgi (Schwartz et al., 1984; Strous et al., 1985; Chapman and Munro, 1994), but the mechanism is not known. To this end, we performed fixed immunostaining of CI-M6PR. We observe strong perinuclear colocalization between CI-M6PR and the Golgi tether GM130 in DMSO, whereas in LLOMe CI-M6PR mis-localized in enlarged compartments within the periphery (Fig. 8 E-G). We further speculated that CI-M6PR would be accumulated in LEs, given that previously reported pH neutralizing treatments led to M6PR accumulation in endosomes, not lysosomes, by electron microscopy (Brown et al., 1986).

To confirm this, we performed endogenous immunostaining for CI-M6PR in Em-Rab7 expression conditions within primary MEFs. This experiment confirmed that compartments containing mis-localized CI-M6PR were largely Rab7-positive and peripheralized (Fig. 8 H-I). Further, CI-M6PR compartments had more Rab7 on them as compared to controls (Fig. 8 J). Together these data suggest that specific Rab7-dependent cargos necessary for lysosomal function are mis-localized following LLOMe-mediated pH neutralization. We suggest that this mis-localization is due to deficits in tubule formation.

Discussion

In summary, the present study finds that pH neutralization as a result of LLOMe treatment significantly impacts the behavior of the endosomal/lysosomal system upstream of damaged lysosomes (Fig. 9). Recent studies using chloroquine- or sirasamine-driven LMP show that 30% of Rab7+ compartments (constituting EEs, LEs, LYS) were damaged. Many of these likely correspond to LYS, but LYS and LEs were not distinguished from each other (Du Rietz et al., 2020). Notably, we used established and carefully defined compartmental markers and showed that early endosomes as well as early and late Golgi cisternae appear unaffected by LLOMe. In contrast, LEs rapidly respond to LLOMe. The acute LE response is characterized by rapid reorganization/swelling as well as pH neutralization with minimal membrane damage, as compared to LYS. LLOMe-mediated pH neutralization led to increased V-ATPase assembly on populations of both undamaged LEs and damaged LYS. Whereas pH neutralization due to vacuolar damage from *Salmonella* infection (Xu et al., 2019) or LLOMe treatment (Cross et al., 2023) assembles V-ATPase for autophagy conjugation, our data implicate V-ATPase assembly as a coordinator of different cytosolic effectors in sterile LYS damage and LE pH neutralization. Specifically, our data show that V-ATPase assembly influences Rab7 membrane stabilization and subsequently activation state, which we found to be further influenced by the ability of Rab7 to bind the dynein adaptor RILP. Our previous data using RILP overexpression showed greatly increased Rab7 recruitment to LEs consistent with RILP-mediated hyperstabilization of Rab7 (Yap et al., 2022). Thus interestingly, our results suggest a link between changes in the luminal endosomal/lysosomal pH and activation of cytosolic Rab7. These data may provide the first insight that Rab7 activity on LEs is subject to regulation by luminal pH via modulating V-ATPase activity when luminal pH is too alkaline. Given its role as a facilitator of endosomal effector function, even modest changes in Rab7 activation as a result of luminal pH sensing can have profound effects on effector binding and ultimately endosomal function important for control of cellular membrane trafficking. Our results have implications for all instances of endosomal/lysosomal neutralization, including genetic disorders, neurodegenerative disease, and the use of lysosomotropic pH-neutralizing therapeutics, such as selective-serotonin reuptake inhibitors (SSRIs) or atypical antipsychotic therapeutics (Kuzu et al., 2017; Kuwahara et al., 2020; Lakpa et al., 2021), which may similarly cause pH neutralization in LEs but not LMP.

Tubulation changes as prominent components of lysosomal damage responses

LLOMe also led to rapid defects in Rab7 tubulation. We speculate that the loss of tubulation results in mis-trafficking of cargos, including accumulation of loaded dextrans and the endogenous Rab7-dependent cargo CI-M6PR. Others have observed lysosomal tubule formation following LLOMe washout (Bhattacharya et al., 2023), which required Rab7 inactivation by the GAP TBC1D15. Extensive tubules marked by the microtubule adaptor JIP4 were also observed in response to long LLOMe treatments (Bonet-Ponce et al., 2020). In contrast, to the appearance of tubules on LYS after extensive damage (>1h LLOMe) (Bonet-Ponce et al. 2020) or LYS tubules formed during recovery from LYS damage (Bhattacharya et al. 2023), we observe an acute loss of Rab7 tubulation in a short temporal window following LLOMe exposure. We speculate that

LLOMe initially disrupts normal Rab7-containing tubules which are likely retrieving membrane receptors that should not enter lysosomes (such as CI-M6PR), but that other Rab7-negative tubulation events with separate function may still occur on these compartments at later times. For example, initial rapid loss of Rab7 tubulation after LLOMe is later followed by slower LLOMe-induced tubulation driven by increased dynein-JIP4-microtubule coupling (Bonet-Ponce et al., 2020). This slower phase of LLOMe-induced tubulation has been proposed to aid in lysosomal reformation (Bonet-Ponce et al., 2020).

We further suggest that the early loss of tubulation we observe partially contributes to the consistent increased size, decreased number, and increased intensity of Rab7 compartments observed in LLOMe. Given the high degree of apparent interactions we observe between Rab7+ compartments in our live imaging experiments (Fig. 2 E , Video 2, Fig. 4 B, Video 4), we speculate that changes in homotypic LE fusion and heterotypic LE-LYS fusion also contribute to this size increase of Rab7+ LEs after LLOMe. It is very difficult to discern fusion events in our movies and we decided against trying to quantify putative fusions. In addition, recent work has started to delineate roles for lipid transport in LYS damage responses (Tan and Finkel, 2022; Radulovic et al., 2022). Interestingly, the cholesterol transport protein ORP1L was recruited to damaged LYS in as little as 5 minutes post-LLOMe, in line with the temporal recruitment of Rab7 in our live imaging studies (Radulovic et al., 2022). ORP1L is a Rab7 effector protein that can both directly bind to Rab7 (Johansson et al., 2005) and form a tripartite complex with RILP (Rocha et al., 2009; Ma et al., 2018), and is thought to contribute to late endosomal positioning in response to cholesterol availability. Thus, in settings of pH neutralization, concomitant Rab7 membrane stabilization by RILP (as described in this study) and ORP1L recruitment (as in Radulovic et al. 2022) appear to facilitate cholesterol transfer, which subsequently might contribute to the altered phenotype of Rab7+ LEs.

A new role for Rab7+ late endosomes in LMP homeostasis and the impact of Rab7 and V-ATPase assembly on damaged lysosomes

We unexpectedly observed rapid recruitment of V1-G1 to damaged LEs and LYS. The potential consequences of LMP-mediated V-ATPase assembly are multifaceted. On undamaged but pH-neutralized LEs, V-ATPase assembly-driven Rab7 activation could serve as an accelerant of endosomal maturation during stress. As V-ATPase assembly and acidification were recently linked to increased degradation in previously quiescent compartments (Ratto et al., 2022), it is possible that this mechanism serves to activate a pool of initially weakly-degradative LEs to generate functional lysosomes in order to maintain proteostasis or aid in lysophagy progression. Future studies are needed to elucidate the definitive downstream role of undamaged, actively acidifying LEs following lysosomal disruption.

In contrast, on LYS with damaged membranes, increased pump activity for the sake of acidification is futile. However, assembled V-ATPase in the setting of membrane damage can also provide roles independent of its function as a proton pump. Notably in *Salmonella* infection, V-ATPase assembly following bacterial driven damage to the membrane of *Salmonella* containing vacuoles (SCVs) recruits ATG16L1 for LC3 lipidation and recognition of the pathogen (Xu et al., 2019). As LC3 is known to accumulate and coordinate subsequent lysosomal responses in LLOMe (Nakamura et al., 2020), and Rab7 membrane association precedes LC3 on phagosomes (Hooper et al., 2022), our data now provide an interesting future avenue of investigation regarding an intermediate role for activated Rab7 in ATG161L recruitment and LC3 lipidation on damaged LYS membranes. Alternatively, V-ATPase mediated control over Rab7 activation may contribute to autophagosomal flux. In support of this, in other contexts Rab7 activation provides control over the selective autophagy of organelles. Specifically, Rab7 association with its GAP TBC1D15 and effector Vps35 provide control over Rab7 activation and mitophagy progression (Jimenez-Orgaz

et al., 2018). Thus, whether the presence of active Rab7 on the damaged membranes due to V-ATPase assembly is ultimately essential for lysophagy progression remains an open question.

Aberrant phosphoinositide homeostasis in LMP may also contribute to V-ATPase behavior and Rab7 hyperactivation. Osmotic challenges in yeast lead to drastic increases in PIP(3,5)P_2 levels and subsequently V-ATPase assembly on the vacuole (Li et al., 2014). Changes in phosphoinositide species therefore might also play an important role. For instance, PI4P is greatly enriched on damaged LYS (Tan and Finkel, 2022; Radulovic et al., 2022), and acute conversion of PI4P to PI(4,5)P_2 was also shown to release GTP-Rab7 from endosomes and disrupt autophagic flux (Baba et al., 2019). Thus, excess PI4P production may contribute to active Rab7 membrane retention. How changes in phosphoinositides might contribute to V-ATPase or Rab7 regulation during LMP await future studies.

Endosomal membrane stabilization of active Rab7 is influenced by V-ATPase assembly and RILP binding: an effector balance?

We found that pH neutralization in LLOMe-induced LMP was sufficient to lead to both changes in Rab7+ compartment size, number and intensity, as well as drive V_1G_1 assembly on endosomal membranes. Though reports previously implicated Rab7-mediated recruitment of RILP to regulate V_1G_1 levels and pump activity, our data demonstrate that Rab7 is not the main driver for V_1G_1 recruitment after LLOMe. In contrast, we find that both general V-ATPase assembly and RILP contribute to Rab7 membrane stabilization and subsequently activation state.

Our FRAP data suggests that assembled proton pumps can partially stabilize Rab7 in settings of luminal endosomal neutralization (compare BafA1 vs. LLOMe or NH_4Cl). Our findings are consistent with the observation that knockout of the integral membrane V_0a_3 subunit in osteoclasts, which disrupts pump assembly, also depletes GTP-bound Rab7 (Matsumoto et al., 2018) and the Rab7 GEF Mon1-Ccz1 (Matsumoto et al., 2022) from endosomal membranes. Notably, BafA1 FRAP phenotypes were partial, in that they did not completely recover Rab7 stability despite lack of V-ATPase assembly, suggesting that parallel pathways to this assembly also contribute to increased Rab7 stabilization in pH-neutralizing conditions. Our FRAP data with $Rab7^{L8A}$ in LLOMe suggest that one such parallel pathway is RILP-binding to Rab7. Previous data from both our lab and others suggested overexpressed RILP massively stabilized Rab7 on membranes (Jordens et al., 2001; Yap et al., 2022). Now, our Em-$Rab7^{L8A}$ FRAP data suggest that loss of RILP binding destabilizes Rab7 on membranes in LLOMe. A direct interaction between Rab7-GDP and V_0a_3 has also been reported (Matsumoto et al. 2018), and might contribute to Rab7 stabilization in addition to a ternary Rab7-RILP-V_1G_1 complex. In the context of our findings, we propose a model whereby the Rab7-RILP axis serves as a conduit for Rab7 delivery to the membrane. V_0a_3 or the assembled pump might then serve to stabilize Rab7-effector complexes or the Rab7-GEF complex, and ultimately activate Rab7. This warrants additional investigation, but collectively would be akin to V-ATPase driven recruitment of the ARF-GEF ARNO for Arf6 activation (Maranda et al., 2001).

Lastly, our data begin to uncover a complex balance of Rab7 effectors on late endosomes that may depend on RILP as the limiting partner. Toggling of Rab7-RILP complexes between V-ATPase subunits and dynein, for instance, might influence predominant acidification or tubulation activities on late endosomes. Given our findings, we speculate that increased pump-related RILP-Rab7 interactions and subsequent Rab7 stabilization sequesters active Rab7 away from effectors like retromer. The observed M6PR mis-sorting might thus be a consequence of a disrupted Rab7 effector balance. Much more work is required to probe this notion in the future.

In summary, the present study finds that pH neutralization as a result of LLOMe treatment not only damages LYS but also has significant upstream functional consequences on LEs. It elicits increased V-ATPase assembly not only on LYS but also on LEs, contributing to Rab7 membrane stabilization and hyperactivation, and defective trafficking of Rab7-dependent

cargos like M6PRs. Our data further raise new questions about Rab7 effector selection and multiplexing, and its connection to luminal pH sensing. This mechanistic link likely underlies dynamic changes in homeostatic endosomal behavior in health and is disrupted in disease. This study therefore broadens our understanding of cellular responses to LE/LYS disruptions and raises new questions regarding how Rab7 and its effectors orchestrate the interplay between endosomal pH, tubulation, and ultimately lysophagy.

Materials and Methods

Immortalized cell line culture and transfection

Normal rat kidney (NRK) cells (ATCC CRL6509) and COS-7 cells (UVA Tissue Culture Facility) were maintained in DMEM with glucose and GlutaMAX (Gibco 10566-016) plus 10% fetal bovine serum (FBS) without antibiotics. All cells were incubated at 37°C and maintained at 5% CO_2. For fixed imaging, cells were plated on coverslips coated with 10 µg/mL fibronectin (Sigma) for 1 hour at 37°C. For live imaging, cells were plated on 35mm dishes with 14mm glass bottom inserts (MatTek) coated with 10µg/mL fibronectin for 1 hour at 37°C. Transfections into NRK and COS-7 cells for use in fixed or live imaging experiments and GST-RILP Rab7 activity pulldowns were performed using Lipofectamine 2000 (Invitrogen) per manufacturer's instructions. Downstream applications were conducted 24 hours post-transfection unless otherwise stated. For establishment of stable Emerald-Rab7-WT and L8A (Em-Rab7) NRK cell lines, Em-Rab7^{WT} or Em-Rab7^{L8A} was transfected into NRK cells. 24 hours post transfection, cells were exposed to and maintained on 100µg/mL geneticin (Gibco) in complete DMEM. After 5 days of selection, individual cell colonies were selected and expanded in geneticin containing medium. Purity of clones was screened for homogenous Em-Rab7 expression by fluorescence microscopy. Pure clones were expanded, frozen, and maintained in geneticin containing DMEM for downstream applications.

Primary mouse embryonic fibroblast isolation and nucleofection

All experiments were performed in accordance with the University of Virginia Institutional Animal Care and Use Committee guidelines and regulations. Primary mouse embryonic fibroblasts (MEFs) were isolated from E13.5 Rab7$^{fl/fl}$ mice (Kawamura et al., 2012) (Riken BioResource Research Center #RBRC05600). Embryos were sterilely isolated from fluid sacs and torsos were isolated by removal of the head, limbs and tail. Internal organs and spinal cord were then removed by forceps. Remaining tissue was triturated in 0.05% trypsin-EDTA then incubated at 37°C for 10 minutes. An equivalent volume of 20% FBS in MEF medium [DMEM with glucose and L-glutamine (Gibco 11965-092)] was then added and the tissue was re-triturated. Cells were then spun, re-suspended, and plated in MEF medium containing 10% FBS for expansion, freezing, or downstream applications. Upon use, MEFs were maintained in MEF medium containing 10% FBS without antibiotics. For single or double plasmid expression experiments (e.g., EmRab7 overexpression or Cre-recombinase knockouts), MEFs were nucleofected using Ingenio Solution electroporation reagent (Mirus Bio) and Lonza AMAXA Nucleofector II. Briefly, 1.5 million MEFs and 5µg total DNA were diluted in 100µL of Ingenio Solution in a 0.2cm cuvette (Mirus). MEFs were nucleofected using AMAXA program A-023 (MEF). Cells were immediately recovered in 900µL of pre-warmed complete MEF medium and then diluted and plated on 10µg/mL fibronectin coated coverslips. For Rab7 knockout experiments, downstream analyses were conducted three days post pCAG-Cre-GFP nucleofection. For live imaging use, MEFs were plated on 35mm dishes with 14mm glass bottom inserts (MatTek) coated with 10µg/mL fibronectin for 1 hour at 37°C.

Plasmids

The plasmids used in this study are as follows:

Emerald-Rab7^{WT} (Addgene #54244, Davidson Lab), GFP-Rab7^{WT} (Addgene #12605, Pagano Lab), GFP-Rab7^{Q67L} (gift from Dr. James Casanova, University of Virginia), GFP-Rab7^{T22N} (Addgene #12660, Pagano Lab), pCAG-Cre-GFP (Addgene #13776, Cepko Lab), pCDNA3-2xHA-V1G1 (gift from Dr. Cecilia Bucci, University of Salento), pET-His-GST-tev-LIC (Addgene #29655, Gradia Lab), pGEX-4T-3-mR7BD (Addgene #79149, Edinger Lab). To generate Emerald-Rab7^{L8A}, Rab7a with a point mutation at residue 8 from leucine to alanine (L8A) was cloned into pEmerald-C1 (Addgene#54734, Davidson Lab) at XhoI-BamHI sites by Genscript, using gene synthesis.

Primary Antibodies

The list of primary antibodies used in this study are as follows: Anti-Rab7 (rabbit monoclonal; 1:100 IF; abcam 137029; RRID:AB_2629474), Anti-Rab7 (rabbit polyclonal; 1:1000 WB; proteintech 55469-1-AP; RRID:AB_11182831), Anti-Cathepsin B (goat polyclonal; 1:200 IF; R&D Systems AF965; RRID: AB_2086949), Anti-Cathepsin D (goat polyclonal; 1:200 IF; R&D Systems AF1029; RRID: AB_2087094), anti-LAMP1 (mouse monoclonal; 1:1000 IF; Enzo Life Sciences ADI-VAM-EN001; RRID:AB_2038958), anti-GM130 (mouse monoclonal; 1:500 IF; BD Biosciences 610822 RRID: AB_398141), anti-TGN38 (mouse monoclonal; 1:200 IF; BD Biosciences 610898, RRID:AB_398215), anti-Vps35 (goat polyclonal; 1:600 IF, 1:2000 WB; abcam 10099; RRID:AB_296841), anti-EEA1 (mouse monoclonal; 1:100 IF; BD Biosciences 610456; RRID: AB_399409), anti-CI-M6PR (rabbit monoclonal; 1:200 IF; abcam 124767; RRID:AB_10974087), anti-ALIX (mouse monoclonal; 1:100 IF; Santa Cruz sc-53540; RRID: AB_673819), anti-Galectin-3 (mouse monoclonal; 1:100 IF; Santa Cruz sc-25279; RRID: AB_627656), anti-Galectin-3 (rat monoclonal; 1:100 IF; Santa Cruz sc-23938; RRID: AB_627658), anti-GFP (rabbit polyclonal; 1:2000 WB; proteintech 50430-2-AP; RRID: AB_11042881), anti-GST (mouse; 1:1000 WB; Santa Cruz sc-138; RRID: AB_627677); anti-HA (mouse monoclonal; 1:100 IF, 1:1000 WB; Santa Cruz sc-7392; RRID: AB_627809); anti-HA (rabbit; 1:100 IF, 1:1000 WB; Santa Cruz sc-805; RRID: AB_631618).

Secondary Antibodies

For immunocytochemistry, the following Alexa Fluor–coupled antibodies from Invitrogen were used: Alexa405-Phalloidin (A30104), Alexa488 donkey anti-mouse (A21202; RRID: AB_2535792), Alexa488 donkey anti-rabbit (A21206; RRID: AB_ 2534102), Alexa488 donkey anti-goat (A11055; RRID: AB_2534013), , Alexa568 donkey anti-mouse (A10037; RRID: AB_2534017), Alexa568 donkey anti-rabbit (A10042, RRID: AB_2534104), Alexa568 donkey anti-goat (A11057; RRID: AB_162546), Alexa647 donkey anti-mouse (A31571; RRID: AB_2536183), Alexa647 donkey anti-rabbit (A31573; RRID: AB_2535864), Alexa647 donkey anti-goat (A21447; RRID: AB_2340373). The following antibodies from Jackson ImmunoResearch Laboratories, Inc. were used: Alexa488 donkey anti-rat (712-545-153; RRID: AB_2340684), Alexa568 donkey anti-rat (712-585-153; RRID: AB_2340689), Alexa647 donkey anti-rat (712-605-153; RRID: AB_2340694), DyLight405 donkey anti-goat (705-475-147; RRID: AB_2340427), DyLight405 donkey anti-rat (712-475-153; RRID: AB_2340681). For western blotting, the following Jackson ImmunoResearch Laboratories, Inc. antibodies were utilized: donkey anti-mouse Alexa680 (715–625-151; RRID: AB_2340869), donkey anti-mouse Alexa800 (715-655-151; RRID: AB_2340871), donkey anti-rabbit Alexa680 (711-625-152; RRID: AB_2340627), donkey anti-rabbit Alexa790 (111-655-144; RRID: AB_2338086).

Immunocytochemistry and image acquisition

Immunocytochemistry was conducted as described in (Mulligan et al., 2023). Briefly, cells were fixed in 4% paraformaldehyde/3% sucrose in PBS at room temperature for 15 minutes. Cells were then blocked and permeabilized using PBS/5% normal donkey serum/0.2% TritonX-100 or 0.1% saponin for 20 minutes at room temperature. Saponin permeabilization was used when staining for lysosomal membrane proteins (e.g., LAMP1, LAMP2); TritonX-100 was used for all others. Primary and secondary antibodies were diluted in 1% bovine serum albumin (BSA)/PBS and incubated for 1 hour and 30 minutes, respectively, at room temperature. 0.1% saponin was included in BSA antibody dilutions when staining for lysosomal membrane proteins. Coverslips were mounted in ProLong Gold antifade mounting medium (Invitrogen).

For widefield imaging, mounted coverslips were viewed using a Zeiss Z1-Observer with a 40x objective (enhanced chemiluminescence Plan-Neofluor 40x/0.9 Pol working distance = 0.41). Apotome structured illumination was used for all images. Images were captured with the Axiocam 503 camera using Zen software (2012 Blue edition, Zeiss) and identically processed in FIJI software. On average, 10 representative fields per condition per experiment were captured, for 3 independent experiments.

For live-cell spinning disk confocal microscopy, live cell imaging dishes were replaced with phenol-red free DMEM (Gibco 31053-028) plus 10% FBS and 1X GlutaMAX (Gibco 35050-061) prior to imaging. Cells were viewed using a temperature-controlled (37°C) Nikon TE 2000 microscope using a 60X/NA1.45 oil objective, equipped with Yokogawa CSU 10 spinning disc and images were captured with a 512X512 Hamamatsu 9100c-13 EM-BT camera. On average, multicolor images were collected at a rate of 1 image/3 seconds for indicated times, with perfect focus on, up to 30 minutes (600 frames,) and compiled using FIJI software. Vehicle (DMSO) or LLOMe (final concentration 1mM) were added in a bolus at 2 minutes (frame 40) live on the stage for all live-imaging experiments. On average, 10-15 movies per condition were collected from 3 independent experiments.

For traditional confocal microscopy, cells plated in live imaging dishes with phenol-red free DMEM (Gibco 31053-028) plus 10% FBS and 1X GlutaMAX (Gibco 35050-061) or mounted coverslips were viewed using a Nikon Ti2-E inverted microscope with AX-R confocal microscopy system and 25 mm FOV resonant scanner/25 mm FOV galvano scanner, with an NSPARC detector unit. The system was controlled and images captured using photomultipliers and the Nikon NIS Elements C software. Cells were viewed using a 60X/NA1.40 oil objective and maintained in a temperature-controlled system at 37°C with perfect focus during live image acquisition. Captured images and movies were identically processed using Elements Denoise.ai followed by compiling in FIJI software. On average, 20-30 movies (FRAP), and 45-60 images (tubulation) per condition were collected from 3 independent experiments.

For Airyscan imaging, mounted coverslips were viewed using the Zeiss 980 NLO system using an inverted Axio Observer microscope with a 63X/NA1.40 oil objective and an 8Y-airyscan detector. Images were collected using Zeiss Zen Blue software on Super-Resolution-4Y mode with 0.13µm z-sections, and z-stacks were identically processed using Zen Airyscan 3-D Processing. On average, 3 representative fields per condition were captured, for 3 independent experiments (approximately 30 total cells per condition).

Lysosomal perturbation treatments

For induction of lysosomal damage, all cells were incubated in complete DMEM or MEF medium with 10% FBS, supplemented with DMSO (vehicle, 0.33%v/v) or L-leucyl-L-leucine dimethyl ester (LLOMe, Sigma) at 1mM for times indicated. DMSO and LLOMe were equilibrated in fresh, pre-warmed (37°C) complete DMEM with 10% FBS prior to addition to cells.

All other treatments were carried out in complete DMEM or MEF medium with 10% FBS. Bafilomycin-A1 (Sigma) was dissolved in DMSO used at a final concentration of 200nM for 2 hours. Ammonium chloride (Fisher) was dissolved in sterile water and used at a final concentration of 20mM for 1 hour. ML-SA1 (Tocris) was dissolved in DMSO and used at a final concentration of 20μM for 5-30 minutes. For calcium chelation experiments, cells were pre-treated with 10μM BAPTA-AM (Tocris) for 30 minutes. Then, cells were treated with fresh medium containing either DMSO or LLOMe in the presence of an additional 10μM BAPTA-AM for indicated times.

Electron Microscopy

NRK cells were grown on 1% fibronectin (in PBS), and 0.1 mg/mL poly-L-lysine (in ddH2O) coated 6mm sapphire disks (Technotrade International) in complete DMEM at 37°C and treated with 45 minutes of DMSO or 1mM LLOMe before immediate cryo-fixation by high pressure freezing (Leica EM ICE High Pressure Freezer), with 20% BSA in DMEM as a cryoprotectant. Samples were freeze substituted for three days in acetone containing 0.2g/mL methylene green (Spectrum Chemical MFG. GRP.), 0.1% uranyl acetate (Polysciences Inc) and 1% osmium tetroxide (Electron Microscopy Sciences) using Leica EM Automatic Freeze Substitution machine (Leica AFS2). Freeze substituted samples were then infiltrated with increasing Epon/Araldite (Electron Microscopy Sciences) in acetone until they were infiltrated with pure Epon/Araldite, over the course of one day. Epon infiltrated samples were embedded in resin and allowed to set for two days at 60°C followed by mounting on dummy resin blocks. Samples were then sectioned at 70nm using an ultramicrotome (Reichert Ultracuts, Leica) and collected onto 0.7% Pioloform (Ted Pella Inc) coated copper slot grids 2mm x 1mm Ø 3.05mm (Electron Microscopy Sciences). Post staining of samples on grids was performed with 2% uranyl acetate in 70% methanol followed by 0.4% lead citrate in ddH2O. Transmission electron micrographs were collected using a Tecnai F20 Transmission Microscope operated at 200kV and captured using a 4K x 4K UltraScan CCD camera.

Live Imaging Assays

Lysosomal pH Collapse Readouts

NRK cells were loaded with 100μg/mL10kDa fluorescein (FITC) dextran plus 100μg/mL 70kDa tetramethylrhodamine (TMR) dextran (Invitrogen) in complete DMEM at 37°C for 16 hours. After washing with 1X DPBS, dextrans were chased to lysosomes for an additional 4 hours at 37°C in phenol red free complete DMEM. Live time lapse images were captured via spinning disk microscopy with LLOMe added on the stage after 2 minutes. Change in cellular FITC fluorescence over time was plotted relative to initial cellular FITC intensity, relative to TMR.

Em-Rab7 Live Imaging of Late Endosomes versus Lysosomes

Stable Em-Rab7^{WT} NRK cells were loaded with 5μg/mL DQ-BSA (Invitrogen) in complete DMEM at 37°C for 16 hours. The following morning, cells were washed with 1X DPBS and chased for 4 hours in complete DMEM at 37°C. DQ-loaded Em-Rab7^{WT} were then imaged at 37°C with spinning disk confocal microscopy, with DMSO or 1mM LLOMe added live on the stage.

pH Collapse of Late Endosomes versus Lysosomes

NRK cells were loaded with 5μg/mL DQ-BSA (Invitrogen) in complete DMEM at 37°C for 16 hours. The following morning, cells were washed with 1X DPBS and then loaded with 100μg/mL10kDa Oregon Green dextran (OGdex) for 2 hours. Following 2 hour OGdex loading,

cells were washed with 1X DPBS and replaced with complete phenol-red free DMEM and imaged with spinning disk confocal microscopy. DMSO or 1mM LLOMe was added live on the stage during movie acquisition.

Dextran tubulation

For Fig. 8 A, MEFs nucleofected with Em-Rab7^{WT} were loaded with 100µg/mL10kDa tetramethylrhodamine (TMR) dextran for 2 hours. After washing with sterile 1X DPBS, the medium was replaced with phenol-red free complete DMEM supplemented with DMSO or 1mM LLOMe for 30 minutes at 37°C. Still images of dynamic tubules were then captured by live confocal microscopy (Nikon Ti2-E with AX-R) immediately following recovery.

For Fig. 8 D and Video 6, MEFs were loaded with 5µg/mL DQ-BSA in complete DMEM at 37°C for 16 hours. The following day, after washing with sterile 1X DPBS, DQ-BSA were chased for 2 hours in phenol-red free complete DMEM at 37°C. Following chase, cells were then loaded with 100µg/mL10kDa fluorescein (FITC) dextran for 30 minutes. FITC dextran was not chased and imaged immediately after washing and replacement with fresh pre-warmed phenol-red free complete DMEM. Live time lapse images were captured via spinning disk microscopy as described with LLOMe added on the stage after 2 minutes.

Magic Red-Cathepsin B

For use of Magic Red Cathepsin-B (ImmunoChemistry Technologies), MR-B stock was prepared as described in manufacturer's protocol and diluted 1:1000 in complete DMEM. Cells were incubated with dilute MR-B for 20 minutes at 37°C. Cells were then sufficiently washed three times with 1X DPBS and replaced with fresh complete phenol red free DMEM. MR-B loaded cells were equilibrated by incubation at 37°C for 5 minutes prior to spinning disk confocal microscopy. Change in cellular MR-B fluorescence over time was plotted relative to initial intensity.

E-64D Treatments

To determine whether protease activity and generation of amino acids is a signal responsible for Rab7 phenotypes, Em-Rab7^{WT} expressing NRK cells were acutely loaded with 20 ug/mL DQ-BSA for 1 hour in complete DMEM. DQ-BSA was then chased for 1 hour at 37˚C in the absence or presence of 200µM E-64D, in complete DMEM. Following washing, fresh pre-warmed phenol-red free complete DMEM was added. Live time lapse images were captured via spinning disk microscopy with 1mM LLOMe added live on the stage after 2 minutes.

Western blotting

Samples containing 1.2X Sample Buffer (Genscript) were separated via SDS-PAGE using 4-12% Bis-Tris (Genscript) in 1X MES Running Buffer (Genscript) according to manufacturer's instructions. Protein was transferred to nitrocellulose membranes (Bio-Rad) using the high molecular weight program of the Trans-Blot Turbo Transfer system (Bio-Rad) according to manufacturer's instructions. Blocking was performed for 1 hour at room temperature with 100% LI-COR Odyssey Blocking Buffer. Primary antibody incubation (4°C, 16 hours) and secondary antibody incubations (22°C, 1 hour) were performed in 50% Odyssey Blocking Buffer/50% TBS + 0.1% Tween-20. Washes were conducted following primary and secondary incubations, 3 times 10 minutes, with excess TBS + 0.1% Tween-20. Blots were visualized and captured using

the LI-COR Odyssey CL-X imaging system with LI-COR ImageStudio software. Densitometry analyses were performed using ImageStudio software.

Rab7 activity assays

Preparation of bead conjugated GST-fusion proteins and GST-RILP based pulldown assays were performed as described in (Romero Rosales et al., 2009). GST fusion proteins (GST-stop and GST-RILP) were transformed and isolated from BL21 *E.coli* and conjugated to Pierce Superflow GST agarose (Thermo Scientific). To probe for Rab7-GTP, COS-7 cells expressing Em-Rab7^{WT} were treated with DMSO or 1mM LLOMe for 1 hour. Cells were collected by scraping in 1mL PBS containing Complete EDTA-free Protease Inhibitor (Roche) and pelleted. Cell pellets were resuspended in 200µL of GST Pulldown Buffer [20mM HEPES pH 7.4, 100mM NaCl, 5mM $MgCl_2$, 1% TX-100, Roche Complete Protease Inhibitors] and incubated on ice for 15 minutes. Samples were then spun at 14,000rpm for 15 minutes at 4°C. Supernatant was collected in a clean tube and quantitated using Micro-BCA Protein Assay Kit. Excess GST-stop and GST-RILP bound beads (150µg per reaction) were pre-equilibrated in GST Pulldown Buffer. 50µg of input lysates were added to pre-equilibrated beads and rotated for 16 hours at 4°C. Beads were then washed three times with GST Pulldown Buffer and re-suspended in 35µL of 1.2X Sample Buffer before visualization by SDS-PAGE and Western blotting for GFP and GST. 5% inputs were loaded in parallel. GST-RILP pulldowns of Em-Rab7^{WT} were normalized to input levels of Em-Rab7^{WT}.

Em-Rab7 Fluorescence Recovery After Photobleaching (FRAP)

Stable Em-Rab7^{WT} or Em-Rab7^{L8A} NRK cells were imaged live at 37°C in complete phenol-red free DMEM using the Nikon Ti2-E inverted microscope with AX-R confocal microscopy system and Nikon elements software. To generate FRAP movies, images were collected for one minute prior to bleaching at 1 frame per 10 seconds using the AX-R resonant scanner. To bleach Em-Rab7+ endosomes/lysosomes, a 33.0625µm^2 area was bleached for 10 seconds using the 488-laser line (laser power = 15) and the AX-R galvano scanner. Images were then collected post-bleach for 4 minutes, at 1 frame per 10 seconds, using the AX-R resonant scanner. All movies were processed identically following collection using Nikon Elements Denoising.ai and subsequent histogram matching bleach correction in FIJI.

Image and Statistical Analyses

All statistical analyses were performed using either R Studio or Prism 9 software. All assumptions were deemed to be met before a selection of a statistical test. Normality of residuals was tested using the Shapiro-Wilk test. Specific tests used are denoted in figure legends and statistical significance was defined as a p value < 0.05. All image analysis was conducted with either Bitplane Imaris 9.3.1 or FIJI (NIH).

Quantification of Rab7 compartment volume and area: Due to a mix of puncta and apparent cytosolic distributions of Rab7, the surface generation tool in Bitplane Imaris 9.3.1 were utilized to define Rab7 compartments. Rab7 surfaces >0µm^2 and <30µm^2 or >0µm^3 and <5µm^3 were filtered for 2-D area calculations and 3-D volumetric analyses, respectively, which eliminated the cytosolic pool and heavily clustered compartments. We confirmed that area and volume bounds filtered the same population of compartments. The number of compartments per cell, average surface size, and average surface fluorescence intensity per unit area for the entire field were reported.

Quantification of Airyscan endosomal marker colocalization: Two marker colocalization was determined using the colocalization function in Bitplane Imaris 9.3.1. Images were equivalently thresholded before determining Pearson's and Mander's correlation coefficients.

Quantification of time-lapse changes in Em-Rab7 area: Em-Rab7 objects and DQ-BSA objects were defined across all timepoints using the region-growing object generation tool in Imaris 9.3.1. Equivalent thresholds were used for creation of DQ and Em-Rab7 objects across movies and conditions, within each replicate. Em-Rab7 objects were then filtered into DQ*lo* and DQ*hi* compartments based on colocalization with created DQ-BSA objects. The average Em-Rab7 object area per field of view was then extracted for each time point and fitted using R-studio. N= 10 (DMSO) and 9 (LLOMe) fields of view from 3 independent experiments.

Quantification of fluorescent dextran de-quenching: De-quenching of total cellular Fluorescein (FITC) following LLOMe treatment (as in Fig. 1 A-C) was determined using Imaris. Whole cell regions of interest were denoted and cropped. FITC dextran objects were then created using the region-growing object generation tool. The average FITC object fluorescence intensity at each time point for each cell was then extracted and normalized to the first frame. Cumulative averages of all movies for each condition were then plotted over time using Prism. De-quenching of Oregon Green dextran (OGdex) fluorescence (as in Fig. 4) was determined using FIJI. Images were first processed using a median filter with a radius of 2 pixels. A binary mask of Oregon Green compartments was created and added to the ROI manager partitioned as individual objects for single frames 2 minutes prior and 3 minutes following DMSO or LLOMe addition. Fluorescence intensities of Oregon Green and DQ-BSA were measured within each ROI at each time point. ROIs were then filtered into DQ*lo* and DQ*hi* compartments (threshold= 10,000 a.u.) and Oregon Green fluorescence was compared within each DQ filtered group using a paired t-test between pre- and post-treatment time points.

Quantification of ALIX+ LEs and LYS: Total ALIX puncta and colocalization of ALIX puncta with Rab7 and CatB was determined using the region-growing object generation tool in Imaris 9.3.1. Individual objects were created for each ALIX, Rab7 and CatB compartment. MatLab dual and triple object colocalization Imaris plugins were utilized to determine colocalized objects with overlapping radius= 1µm. Colocalization is expressed as the percentage of total Rab7 only, CatB only, or Rab7/CatB dual positive objects that colocalize with an ALIX object.

Quantification of ALIX responsiveness in BAPTA-AM: ALIX puncta and intensity in the presence or absence of Ca^{2+} chelation was quantitated using FIJI. Images were first processed using a median filter with a radius of 2 pixels. A binary mask of ALIX space was created in FIJI and applied to the original image as ROIs. The number of ROIs and average measured intensity of the ROIs were then extracted and reported.

Quantification of HA-V_1G_1 compartments: HA-V_1G_1 puncta number, intensity, and area was calculated using FIJI. All images were first processed using a median filter with a radius of 2 pixels. To determine HA-V_1G_1 intensity on endogenous Rab7 space (Fig. 6 B), a binary mask of Rab7 area was first created. The mask was refined by then eliminating the nucleus and highly clustered Rab7 perinuclear regions which are non-permissive to distinguishing individual compartments. The refined binary mask was applied to the original image as individual ROIs and the fluorescence intensity of HA-V_1G_1 was then measured. Measured HA-V_1G_1 intensity was then normalized to the Rab7 ROI area and reported. To determine the HA-V_1G_1 puncta number and area (as in Fig. 6 E-F and Fig. S4 D-E), a binary mask of HA-V_1G_1 was created and similarly refined by eliminating the nuclear and highly clustered perinuclear regions. The mask was then applied to the original image as individual ROIs and the total number and area of individual ROIs was determined. The number and average area of all HA-V_1G_1 ROIs was then reported.

FRAP Quantification: FRAP movies were equivalently processed using Nikon Elements Denoising.ai followed by Histogram Matching bleach corrections in FIJI. Using FIJI, the fluorescence intensity over time within the bleached area and an equivalently sized ROI control

area was measured. Measurements within the bleached area were affinely scaled by subtracting the minimum intensity within the bleached area intensity from the bleached and control area intensity. Average intensity values at each time point were then plotted. FRAP recovery curves, starting at t= 70s, were fitted using least squares fit, with a one-phase exponential association equation in Prism. $t_{1/2}$ and plateau values were reported. Y_{max} values were calculated as the intensity of the bleached area at t = 300s, and compared across conditions using an ordinary One-Way ANOVA.

Rab7 Tubulation Quantification: EmRab7 tubulation in MEFs was quantified manually in FIJI. Images across conditions were randomized and blinded. Tubules were manually traced using the line tool in FIJI using the Rab7 channel, and confirmed to contain dextran prior to addition to the ROI manager. Tubules were defined as lighter linear membrane extensions emanating from a darker source endosome. Homogenous streaks were not counted due to the possibility of these being highly motile compartments. Total tubule ROIs from each cell were then measured for their length. The number and average length per cell was then reported.

Quantification of CI-M6PR Puncta: CI-M6PR puncta number and Rab7 intensity were quantified in FIJI. The CI-M6PR channel for all images was first processed using a median filter with a radius of 2 pixels, then masked. To determine the number of M6PR compartments, the mask was refined to eliminate the nuclear and highly clustered perinuclear regions which are non-permissive to distinguishing individual compartments. The number of remaining individual C-M6PR ROIs was then counted and reported. To determine the intensity of Rab7 on CI-M6PR space, the unrefined CI-M6PR mask was applied to the un-processed Rab7 channel and the fluorescence intensity of Rab7 was measured. The average Rab7 intensity across ROIs was then calculated for each cell, and subsequently divided by the total CI-M6PR area to provide a value of Average Rab7 intensity per unit CI-M6PR area.

Data Availability

Data available upon request.

Acknowledgements

This work was supported by NIH R01NS083378 and R21NS128756 awarded to B.W., NIH T32GM007267 awarded to the UVA MSTP (PI-D.K.), NIH T32GM139787 awarded to the UVA Cell and Molecular Biology Training Grant (PI-P.T.S.), and NIH F30AG079497 awarded to R.J.M. We acknowledge the Keck Center for Cellular Imaging for the usage of the Zeiss 980 imaging system for generation of Airyscan data (PI-A.P.; NIH-OD025156), and the Casanova and DeSimone labs for the usage of the Nikon TE 2000 spinning disk and Nikon AXR confocal microscopes, in addition to their critiques and support. We also acknowledge the UVA Molecular Electron Microscopy Core (RRID:SCR_019031) for their assistance. We acknowledge Jermaine Austin for his assistance with Gal3 quantification. We again thank Dr. Cecilia Bucci for generously sharing the HA-V_1G_1 plasmid. We thank Dr. David Castle, Dr. James Casanova, Dr. Christopher Bott, Jonathon Sewell, and Isaiah Swann for critical reading of the manuscript.

Model figures (Fig. 2 A, Fig. 5 A, Fig. S3 A, Fig. 9) were created with Biorender.com.

Author Contributions

R.J.M., C.C.Y., and B.W. conceived and coordinated completion of the study. M.M. and S.R. conceived, collected data, and interpreted electron microscopy data. R.J.M. collected and performed data analysis on all data. R.J.M prepared figures and R.J.M and B.W. prepared the first draft of the manuscript. Manuscript editing was performed by R.J.M., M.M., C.C.Y, S.R. and B.W.

Author Notes

Disclosures: The authors declare no conflicts of interest.

References

Baba, T., D.J. Toth, N. Sengupta, Y.J. Kim, and T. Balla. 2019. Phosphatidylinositol 4,5-bisphosphate controls Rab7 and PLEKHM1 membrane cycling during autophagosome-lysosome fusion. *EMBO J.* 38:e100312. doi:10.15252/embj.2018100312.

Bhattacharya, A., R. Mukherjee, S.K. Kuncha, M.E. Brunstein, R. Rathore, S. Junek, C. Münch, and I. Dikic. 2023. A lysosome membrane regeneration pathway depends on TBC1D15 and autophagic lysosomal reformation proteins. *Nat. Cell Biol.* doi:10.1038/s41556-023-01125-9.

Bohannon, K.P., and P.I. Hanson. 2020. ESCRT puts its thumb on the nanoscale: Fixing tiny holes in endolysosomes. *Curr. Opin. Cell Biol.* 65:122–130. doi:10.1016/j.ceb.2020.06.002.

Bonet-Ponce, L., A. Beilina, C.D. Williamson, E. Lindberg, J.H. Kluss, S. Saez-Atienzar, N. Landeck, R. Kumaran, A. Mamais, C.K.E. Bleck, Y. Li, and M.R. Cookson. 2020. LRRK2 mediates tubulation and vesicle sorting from lysosomes. *Sci. Adv.* 6. doi:10.1126/sciadv.abb2454.

Brown, W.J., J. Goodhouse, and M.G. Farquhar. 1986. Mannose-6-phosphate receptors for lysosomal enzymes cycle between the Golgi complex and endosomes. *J. Cell Biol.* 103:1235–1247. doi:10.1083/jcb.103.4.1235.

Bucci, C., P. Thomsen, P. Nicoziani, J. McCarthy, and B. van Deurs. 2000. Rab7: a key to lysosome biogenesis. *Mol. Biol. Cell*. 11:467–480. doi:10.1091/mbc.11.2.467.

Chadwick, S.R., S. Grinstein, and S.A. Freeman. 2021. From the inside out: Ion fluxes at the centre of endocytic traffic. *Curr. Opin. Cell Biol.* 71:77–86. doi:10.1016/j.ceb.2021.02.006.

Chapman, R.E., and S. Munro. 1994. Retrieval of TGN proteins from the cell surface requires endosomal acidification. *EMBO J.* 13:2305–2312. doi:10.1002/j.1460-2075.1994.tb06514.x.

Clapham, D.E. 2007. Calcium signaling. *Cell*. 131:1047–1058. doi:10.1016/j.cell.2007.11.028.

Collins, M.P., and M. Forgac. 2020. Regulation and function of V-ATPases in physiology and disease. *Biochim. Biophys. Acta Biomembr.* 1862:183341. doi:10.1016/j.bbamem.2020.183341.

Cross, J., J. Durgan, D.G. McEwan, and O. Florey. 2023. Lysosome damage triggers direct ATG8 conjugation and ATG2 engagement via CASM. *BioRxiv*. doi:10.1101/2023.03.22.533754.

Dilsizoglu Senol, A., M. Samarani, S. Syan, C.M. Guardia, T. Nonaka, N. Liv, P. Latour-Lambert, M. Hasegawa, J. Klumperman, J.S. Bonifacino, and C. Zurzolo. 2021. α-Synuclein fibrils subvert lysosome structure and function for the propagation of protein misfolding between cells through tunneling nanotubes. *PLoS Biol.* 19:e3001287. doi:10.1371/journal.pbio.3001287.

Eriksson, I., P. Wäster, and K. Öllinger. 2020. Restoration of lysosomal function after damage is accompanied by recycling of lysosomal membrane proteins. *Cell Death Dis.* 11:370. doi:10.1038/s41419-020-2527-8.

Flavin, W.P., L. Bousset, Z.C. Green, Y. Chu, S. Skarpathiotis, M.J. Chaney, J.H. Kordower, R. Melki, and E.M. Campbell. 2017. Endocytic vesicle rupture is a conserved mechanism of cellular invasion by amyloid proteins. *Acta Neuropathol.* 134:629–653. doi:10.1007/s00401-017-1722-x.

Freeman, D., R. Cedillos, S. Choyke, Z. Lukic, K. McGuire, S. Marvin, A.M. Burrage, S. Sudholt, A. Rana, C. O'Connor, C.M. Wiethoff, and E.M. Campbell. 2013. Alpha-synuclein induces lysosomal rupture and cathepsin dependent reactive oxygen species following endocytosis. *PLoS One*. 8:e62143. doi:10.1371/journal.pone.0062143.

Freeman, S.A., S. Grinstein, and J. Orlowski. 2023. Determinants, maintenance, and function of organellar pH. *Physiol. Rev.* 103:515–606. doi:10.1152/physrev.00009.2022.

Hooper, K.M., E. Jacquin, T. Li, J.M. Goodwin, J.H. Brumell, J. Durgan, and O. Florey. 2022. V-ATPase is a universal regulator of LC3-associated phagocytosis and non-canonical autophagy. *J. Cell Biol.* 221. doi:10.1083/jcb.202105112.

Hurtado-Lorenzo, A., M. Skinner, J. El Annan, M. Futai, G.-H. Sun-Wada, S. Bourgoin, J. Casanova, A. Wildeman, S. Bechoua, D.A. Ausiello, D. Brown, and V. Marshansky. 2006. V-ATPase interacts with ARNO and Arf6 in early endosomes and regulates the protein degradative pathway. *Nat. Cell Biol.* 8:124–136. doi:10.1038/ncb1348.

Jia, J., A. Claude-Taupin, Y. Gu, S.W. Choi, R. Peters, B. Bissa, M.H. Mudd, L. Allers, S. Pallikkuth, K.A. Lidke, M. Salemi, B. Phinney, M. Mari, F. Reggiori, and V. Deretic. 2020a. Galectin-3 Coordinates a Cellular System for Lysosomal Repair and Removal. *Dev. Cell*. 52:69–87.e8. doi:10.1016/j.devcel.2019.10.025.

Jia, J., A. Claude-Taupin, Y. Gu, S.W. Choi, R. Peters, B. Bissa, M.H. Mudd, L. Allers, S. Pallikkuth, K.A. Lidke, M. Salemi, B. Phinney, M. Mari, F. Reggiori, and V. Deretic. 2020b. MERIT, a cellular system coordinating lysosomal repair, removal and replacement. *Autophagy*. 16:1539–1541. doi:10.1080/15548627.2020.1779451.

Jimenez-Orgaz, A., A. Kvainickas, H. Nägele, J. Denner, S. Eimer, J. Dengjel, and F. Steinberg. 2018. Control of RAB7 activity and localization through the retromer-TBC1D5 complex enables RAB7-dependent mitophagy. *EMBO J.* 37:235–254. doi:10.15252/embj.201797128.

Johansson, M., M. Lehto, K. Tanhuanpää, T.L. Cover, and V.M. Olkkonen. 2005. The oxysterol-binding protein homologue ORP1L interacts with Rab7 and alters functional properties of late endocytic compartments. *Mol. Biol. Cell*. 16:5480–5492. doi:10.1091/mbc.E05-03-0189.

Jordens, I., M. Fernandez-Borja, M. Marsman, S. Dusseljee, L. Janssen, J. Calafat, H. Janssen, R. Wubbolts, and J. Neefjes. 2001. The Rab7 effector protein RILP controls lysosomal transport by inducing the recruitment of dynein-dynactin motors. *Curr. Biol.* 11:1680–1685. doi:10.1016/s0960-9822(01)00531-0.

Kawamura, N., G.-H. Sun-Wada, M. Aoyama, A. Harada, S. Takasuga, T. Sasaki, and Y. Wada. 2012. Delivery of endosomes to lysosomes via microautophagy in the visceral endoderm of mouse embryos. *Nat. Commun.* 3:1071. doi:10.1038/ncomms2069.

Kirkegaard, T., A.G. Roth, N.H.T. Petersen, A.K. Mahalka, O.D. Olsen, I. Moilanen, A. Zylicz, J. Knudsen, K. Sandhoff, C. Arenz, P.K.J. Kinnunen, J. Nylandsted, and M. Jäättelä. 2010. Hsp70 stabilizes lysosomes and reverts Niemann-Pick disease-associated lysosomal pathology. *Nature*. 463:549–553. doi:10.1038/nature08710.

Klionsky, D.J., Z. Elazar, P.O. Seglen, and D.C. Rubinsztein. 2008. Does bafilomycin A1 block the fusion of autophagosomes with lysosomes? *Autophagy*. 4:849–850.

Kuwahara, T., K. Funakawa, T. Komori, M. Sakurai, G. Yoshii, T. Eguchi, M. Fukuda, and T. Iwatsubo. 2020. Roles of lysosomotropic agents on LRRK2 activation and Rab10 phosphorylation. *Neurobiol. Dis.* 145:105081. doi:10.1016/j.nbd.2020.105081.

Kuzu, O.F., M. Toprak, M.A. Noory, and G.P. Robertson. 2017. Effect of lysosomotropic molecules on cellular homeostasis. *Pharmacol. Res.* 117:177–184. doi:10.1016/j.phrs.2016.12.021.

Lakpa, K.L., N. Khan, Z. Afghah, X. Chen, and J.D. Geiger. 2021. Lysosomal stress response (LSR): physiological importance and pathological relevance. *J Neuroimmune Pharmacol*. 16:219–237. doi:10.1007/s11481-021-09990-7.

Li, S.C., T.T. Diakov, T. Xu, M. Tarsio, W. Zhu, S. Couoh-Cardel, L.S. Weisman, and P.M. Kane. 2014. The signaling lipid PI(3,5)P_2 stabilizes V_1-V(o) sector interactions and activates the V-ATPase. *Mol. Biol. Cell*. 25:1251–1262. doi:10.1091/mbc.E13-10-0563.

De Luca, M., L. Cogli, C. Progida, V. Nisi, R. Pascolutti, S. Sigismund, P.P. Di Fiore, and C. Bucci. 2014. RILP regulates vacuolar ATPase through interaction with the V1G1 subunit. *J. Cell Sci.* 127:2697–2708. doi:10.1242/jcs.142604.

Ma, X., K. Liu, J. Li, H. Li, J. Li, Y. Liu, C. Yang, and H. Liang. 2018. A non-canonical GTPase interaction enables ORP1L-Rab7-RILP complex formation and late endosome positioning. *J. Biol. Chem.* 293:14155–14164. doi:10.1074/jbc.RA118.001854.

Maranda, B., D. Brown, S. Bourgoin, J.E. Casanova, P. Vinay, D.A. Ausiello, and V. Marshansky. 2001. Intra-endosomal pH-sensitive recruitment of the Arf-nucleotide exchange factor ARNO and Arf6 from cytoplasm to proximal tubule endosomes. *J. Biol. Chem.* 276:18540–18550. doi:10.1074/jbc.M011577200.

Markworth, R., V. Dambeck, L.M. Steinbeck, A. Koufali, B. Bues, T.M. Dankovich, C. Wichmann, and K. Burk. 2021. Tubular microdomains of Rab7-endosomes retrieve TrkA, a mechanism disrupted in Charcot-Marie-Tooth 2B. *J. Cell Sci.* doi:10.1242/jcs.258559.

Marshansky, V. 2007. The V-ATPase a2-subunit as a putative endosomal pH-sensor. *Biochem. Soc. Trans.* 35:1092–1099. doi:10.1042/BST0351092.

Matsumoto, N., M. Sekiya, G.-H. Sun-Wada, Y. Wada, and M. Nakanishi-Matsui. 2022. The lysosomal V-ATPase a3 subunit is involved in localization of Mon1-Ccz1, the GEF for Rab7, to secretory lysosomes in osteoclasts. *Sci. Rep.* 12:8455. doi:10.1038/s41598-022-12397-w.

Matsumoto, N., M. Sekiya, K. Tohyama, E. Ishiyama-Matsuura, G.-H. Sun-Wada, Y. Wada, M. Futai, and M. Nakanishi-Matsui. 2018. Essential Role of the a3 Isoform of V-ATPase in Secretory Lysosome Trafficking via Rab7 Recruitment. *Sci. Rep.* 8:6701. doi:10.1038/s41598-018-24918-7.

McCray, B.A., E. Skordalakes, and J.P. Taylor. 2010. Disease mutations in Rab7 result in unregulated nucleotide exchange and inappropriate activation. *Hum. Mol. Genet.* 19:1033–1047. doi:10.1093/hmg/ddp567.

Mrakovic, A., J.G. Kay, W. Furuya, J.H. Brumell, and R.J. Botelho. 2012. Rab7 and Arl8 GTPases are necessary for lysosome tubulation in macrophages. *Traffic*. 13:1667–1679. doi:10.1111/tra.12003.

Mulligan, R.J., C.C. Yap, and B. Winckler. 2023. Endosomal Transport to Lysosomes and the Trans-Golgi Network in Neurons and Other Cells: Visualizing Maturational Flux. *Methods Mol. Biol.* 2557:595–618. doi:10.1007/978-1-0716-2639-9_36.

Nakamura, S., S. Shigeyama, S. Minami, T. Shima, S. Akayama, T. Matsuda, A. Esposito, G. Napolitano, A. Kuma, T. Namba-Hamano, J. Nakamura, K. Yamamoto, M. Sasai, A. Tokumura, M. Miyamoto, Y. Oe, T. Fujita, S. Terawaki, A. Takahashi, M. Hamasaki, M. Yamamoto, Y. Okada, M. Komatsu, T. Nagai, Y. Takabatake, H. Xu, Y. Isaka, A. Ballabio, and T. Yoshimori. 2020. LC3 lipidation is essential for TFEB activation during the lysosomal damage response to kidney injury. *Nat. Cell Biol.* 22:1252–1263. doi:10.1038/s41556-020-00583-9.

Nakanishi-Matsui, M., and N. Matsumoto. 2022. V-ATPase a3 Subunit in Secretory Lysosome Trafficking in Osteoclasts. *Biol. Pharm. Bull.* 45:1426–1431. doi:10.1248/bpb.b22-00371.

Niekamp, P., F. Scharte, T. Sokoya, L. Vittadello, Y. Kim, Y. Deng, E. Südhoff, A. Hilderink, M. Imlau, C.J. Clarke, M. Hensel, C.G. Burd, and J.C.M. Holthuis. 2022. Ca2+-activated sphingomyelin scrambling and turnover mediate ESCRT-independent lysosomal repair. *Nat. Commun.* 13:1875. doi:10.1038/s41467-022-29481-4.

Papadopoulos, C., B. Kravic, and H. Meyer. 2020. Repair or Lysophagy: Dealing with Damaged Lysosomes. *J. Mol. Biol.* 432:231–239. doi:10.1016/j.jmb.2019.08.010.

Polanco, J.C., and J. Götz. 2021. Exosomal and vesicle-free tau seeds - propagation and convergence in endolysosomal permeabilization. *FEBS J.* doi:10.1111/febs.16055.

Radulovic, M., K.O. Schink, E.M. Wenzel, V. Nähse, A. Bongiovanni, F. Lafont, and H. Stenmark. 2018. ESCRT-mediated lysosome repair precedes lysophagy and promotes cell survival. *EMBO J.* 37. doi:10.15252/embj.201899753.

Radulovic, M., E.M. Wenzel, S. Gilani, L.K. Holland, A.H. Lystad, S. Phuyal, V.M. Olkkonen, A. Brech, M. Jäättelä, K. Maeda, C. Raiborg, and H. Stenmark. 2022. Cholesterol transfer via endoplasmic reticulum contacts mediates lysosome damage repair. *EMBO J.* 41:e112677. doi:10.15252/embj.2022112677.

Ratto, E., S.R. Chowdhury, N.S. Siefert, M. Schneider, M. Wittmann, D. Helm, and W. Palm. 2022. Direct control of lysosomal catabolic activity by mTORC1 through regulation of V-ATPase assembly. *Nat. Commun.* 13:4848. doi:10.1038/s41467-022-32515-6.

Repnik, U., M. Borg Distefano, M.T. Speth, M.Y.W. Ng, C. Progida, B. Hoflack, J. Gruenberg, and G. Griffiths. 2017. L-leucyl-L-leucine methyl ester does not release cysteine cathepsins to the cytosol but inactivates them in transiently permeabilized lysosomes. *J. Cell Sci.* 130:3124–3140. doi:10.1242/jcs.204529.

Du Rietz, H., H. Hedlund, S. Wilhelmson, P. Nordenfelt, and A. Wittrup. 2020. Imaging small molecule-induced endosomal escape of siRNA. *Nat. Commun.* 11:1809. doi:10.1038/s41467-020-15300-1.

Rocha, N., C. Kuijl, R. van der Kant, L. Janssen, D. Houben, H. Janssen, W. Zwart, and J. Neefjes. 2009. Cholesterol sensor ORP1L contacts the ER protein VAP to control Rab7-RILP-p150 Glued and late endosome positioning. *J. Cell Biol.* 185:1209–1225. doi:10.1083/jcb.200811005.

Romero Rosales, K., E.R. Peralta, G.G. Guenther, S.Y. Wong, and A.L. Edinger. 2009. Rab7 activation by growth factor withdrawal contributes to the induction of apoptosis. *Mol. Biol. Cell*. 20:2831–2840. doi:10.1091/mbc.E08-09-0911.

Schwartz, A.L., A. Bolognesi, and S.E. Fridovich. 1984. Recycling of the asialoglycoprotein receptor and the effect of lysosomotropic amines in hepatoma cells. *J. Cell Biol.* 98:732–738. doi:10.1083/jcb.98.2.732.

Shao, E., and M. Forgac. 2004. Involvement of the nonhomologous region of subunit A of the yeast V-ATPase in coupling and in vivo dissociation. *J. Biol. Chem.* 279:48663–48670. doi:10.1074/jbc.M408278200.

Skowyra, M.L., P.H. Schlesinger, T.V. Naismith, and P.I. Hanson. 2018. Triggered recruitment of ESCRT machinery promotes endolysosomal repair. *Science*. 360. doi:10.1126/science.aar5078.

Stransky, L.A., and M. Forgac. 2015. Amino Acid Availability Modulates Vacuolar H+-ATPase Assembly. *J. Biol. Chem.* 290:27360–27369. doi:10.1074/jbc.M115.659128.

Strous, G.J., A. Du Maine, J.E. Zijderhand-Bleekemolen, J.W. Slot, and A.L. Schwartz. 1985. Effect of lysosomotropic amines on the secretory pathway and on the recycling of the asialoglycoprotein receptor in human hepatoma cells. *J. Cell Biol.* 101:531–539. doi:10.1083/jcb.101.2.531.

Tan, J.X., and T. Finkel. 2022. A phosphoinositide signalling pathway mediates rapid lysosomal repair. *Nature*. 609:815–821. doi:10.1038/s41586-022-05164-4.

Thiele, D.L., and P.E. Lipsky. 1990. Mechanism of L-leucyl-L-leucine methyl ester-mediated killing of cytotoxic lymphocytes: dependence on a lysosomal thiol protease, dipeptidyl peptidase I, that is enriched in these cells. *Proc. Natl. Acad. Sci. USA*. 87:83–87. doi:10.1073/pnas.87.1.83.

Uchimoto, T., H. Nohara, R. Kamehara, M. Iwamura, N. Watanabe, and Y. Kobayashi. 1999. Mechanism of apoptosis induced by a lysosomotropic agent, L-Leucyl-L-Leucine methyl ester. *Apoptosis*. 4:357–362. doi:10.1023/a:1009695221038.

Wang, F., R. Gómez-Sintes, and P. Boya. 2018. Lysosomal membrane permeabilization and cell death. *Traffic*. 19:918–931. doi:10.1111/tra.12613.

Wang, R., J. Wang, A. Hassan, C.-H. Lee, X.-S. Xie, and X. Li. 2021. Molecular basis of V-ATPase inhibition by bafilomycin A1. *Nat. Commun.* 12:1782. doi:10.1038/s41467-021-22111-5.

Wu, M., T. Wang, E. Loh, W. Hong, and H. Song. 2005. Structural basis for recruitment of RILP by small GTPase Rab7. *EMBO J.* 24:1491–1501. doi:10.1038/sj.emboj.7600643.

Xu, Y., P. Zhou, S. Cheng, Q. Lu, K. Nowak, A.-K. Hopp, L. Li, X. Shi, Z. Zhou, W. Gao, D. Li, H. He, X. Liu, J. Ding, M.O. Hottiger, and F. Shao. 2019. A Bacterial Effector Reveals the V-ATPase-ATG16L1 Axis that Initiates Xenophagy. *Cell*. 178:552–566.e20. doi:10.1016/j.cell.2019.06.007.

Yang, H., and J.X. Tan. 2023. Lysosomal quality control: molecular mechanisms and therapeutic implications. *Trends Cell Biol.* doi:10.1016/j.tcb.2023.01.001.

Yap, C.C., L. Digilio, L.P. McMahon, A.D.R. Garcia, and B. Winckler. 2018. Degradation of dendritic cargos requires Rab7-dependent transport to somatic lysosomes. *J. Cell Biol.* 217:3141–3159. doi:10.1083/jcb.201711039.

Yap, C.C., L. Digilio, L.P. McMahon, T. Wang, and B. Winckler. 2022. Dynein Is Required for Rab7-Dependent Endosome Maturation, Retrograde Dendritic Transport, and Degradation. *J. Neurosci.* 42:4415–4434. doi:10.1523/JNEUROSCI.2530-21.2022.

Yim, W.W.-Y., H. Yamamoto, and N. Mizushima. 2022. Annexins A1 and A2 are recruited to larger lysosomal injuries independently of ESCRTs to promote repair. *FEBS Lett.* doi:10.1002/1873-3468.14329.

Zoncu, R., and R.M. Perera. 2022. Built to last: lysosome remodeling and repair in health and disease. *Trends Cell Biol.* 32:597–610. doi:10.1016/j.tcb.2021.12.009.

Figure 1

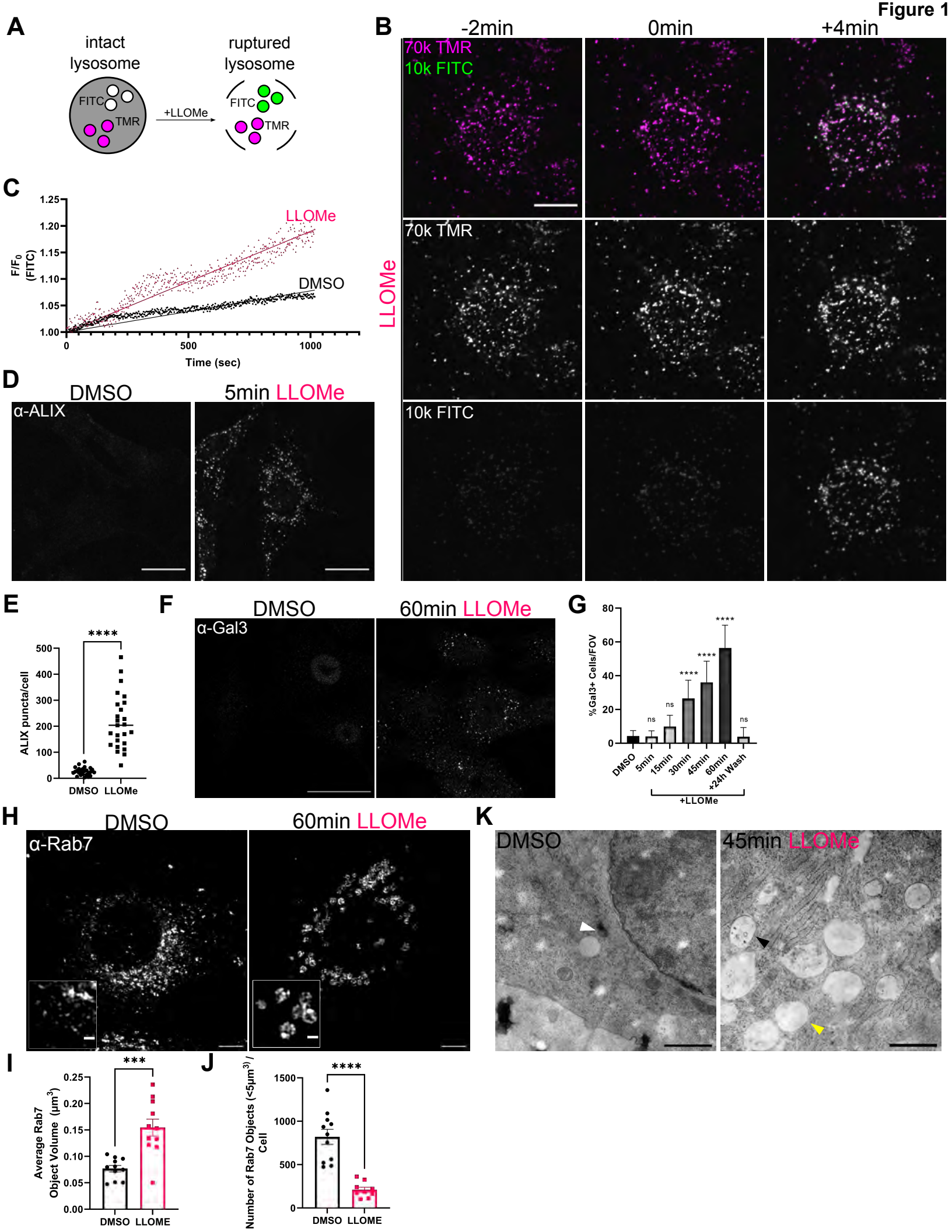
A
intact lysosome
ruptured lysosome
FITC
TMR
+LLOMe
B
-2min
0min
+4min
70k TMR
10k FITC
LLOMe
C
LLOMe
DMSO
F/F0 (FITC)
Time (sec)
D
DMSO
5min LLOMe
α-ALIX
E
ALIX puncta/cell
DMSO
LLOMe
F
DMSO
60min LLOMe
α-Gal3
G
%Gal3+ Cells/FOV
DMSO
5min
15min
30min
45min
60min
+24h Wash
+LLOMe
H
DMSO
60min LLOMe
α-Rab7
K
DMSO
45min LLOMe
I
Average Rab7 Object Volume (μm3)
DMSO
LLOME
J
Number of Rab7 Objects (<5μm3) / Cell
DMSO
LLOME

Figure 1 LLOMe disrupts organelles leading to membrane repair, lysophagy, and responses in Rab7-positive vesicles

(A) Schematic of pH dextran experiment: lysosomes were dually loaded with 100µg/mL pH sensitive 10 kDa FITC-dextran and pH-insensitive 10 kDa TMR-dextran. Lysosomal disruption with LLOMe de-quenches FITC fluorescence.

(B, C) Representative time-lapse images (see *Video 1*) of NRK cells loaded with dual dextrans and exposed to LLOMe at t=0 min (scale=10µm) (B). Change in FITC fluorescence of the experiment in (B) quantified over time and fitted linearly (n=9 movies per condition from 3 independent experiments) (C)**.**

(D, E) Primary mouse embryonic fibroblasts (MEFs) treated with vehicle (DMSO) or 1mM LLOMe for 5 minutes were immunostained for ESCRT associated protein ALIX (scale=25µm) (D). Number of ALIX puncta per cell were quantified and compared using Welch's t-test (n= 24 FOV from 3 independent experiments, ****p<0.0001) (E).

(F, G) NRK cells were treated with vehicle (DMSO) or 1mM LLOMe for one hour and immunostained for galectin-3 (Gal3) (scale= 25µm) (F). The percentage of Gal3+ cells per field of view were quantified over time. (G). A washout condition was included to show that cells will clear damaged lysosomes in NRK cells, similar to what is reported for other cell lines. LLOMe treated time points were compared to vehicle (DMSO) using One-Way ANOVA (n= 30 FOV per condition from 3 independent experiments, *p<0.05, **p<0.01, ***p<0.001, ****p<0.0001. Error bars indicate SEM).

(H) Normal rat kidney cells (NRK) were immunostained for Rab7 following vehicle (DMSO) or 1mM LLOMe treatment for one hour (scale= 5µm, inset = 1µm) and imaged by Airyscan microscopy. Average Rab7 object volume **(I)** and number **(J)** per cell were determined using Imaris and compared using Mann-Whitney U Test (n= 55 cells from 10 FOV per condition, from 3 independent experiments, ***p<0.001, ****p<0.0001. Error bars indicate SEM.)

(K) Representative transmission electron micrographs of vehicle (DMSO) and 1mM LLOMe treated NRK cells (70nm sections, scale=2µm, from 1 experiment). Highly electron dense vesicle (lysosome), indicated with white arrowhead in DMSO (*left*). Single membraned, enlarged, lucent structures with (black) and without (yellow) luminal contents indicated in LLOMe (*right*).

Figure 2

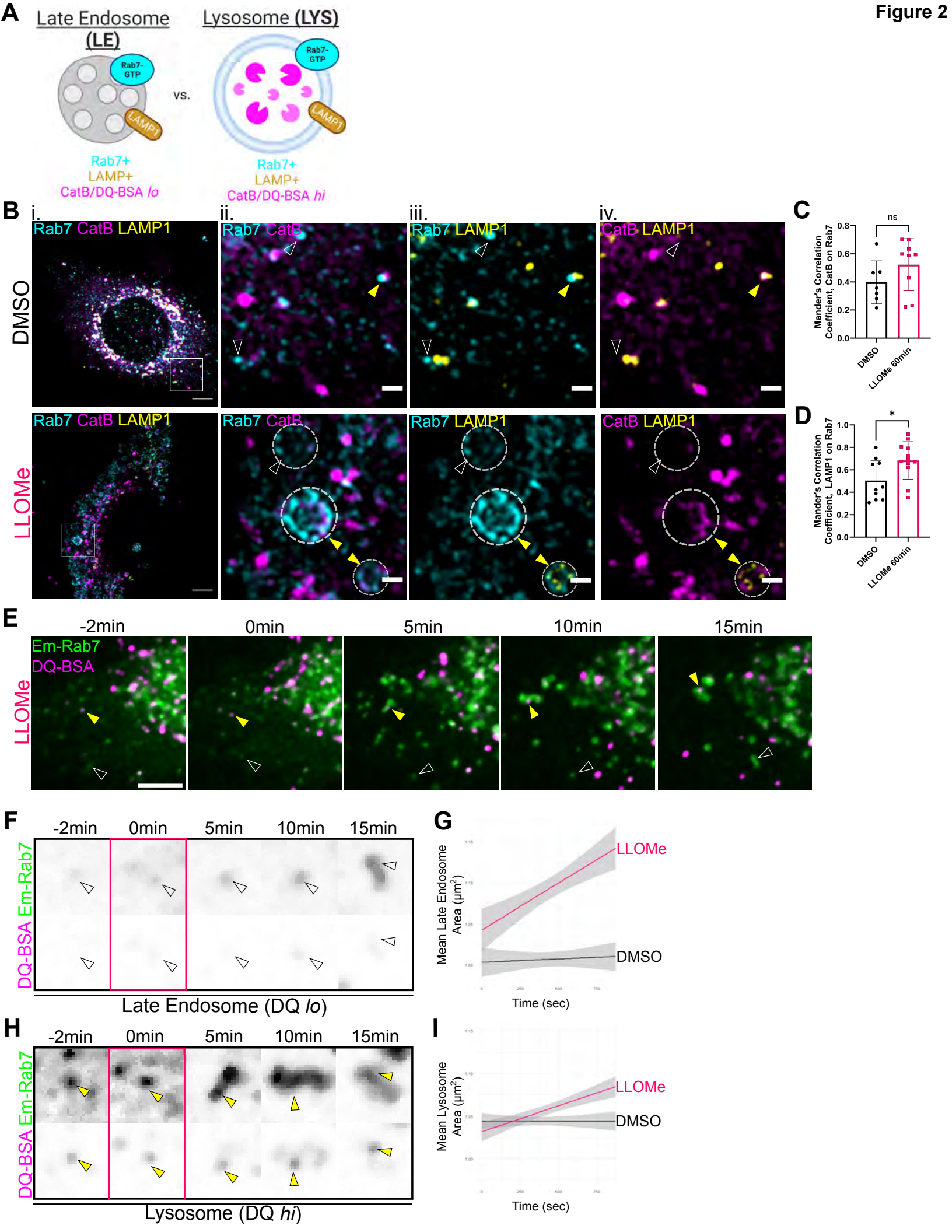
A
Late Endosome (LE)
Lysosome (LYS)
Rab7-GTP
LAMP1
vs.
Rab7+
LAMP+
CatB/DQ-BSA lo
CatB/DQ-BSA hi
B
i.
ii.
iii.
iv.
Rab7 CatB LAMP1
Rab7 CatB
Rab7 LAMP1
CatB LAMP1
DMSO
LLOMe
C
Mander's Correlation Coefficient, CatB on Rab7
ns
DMSO
LLOMe 60min
D
Mander's Correlation Coefficient, LAMP1 on Rab7
*
E
-2min
0min
5min
10min
15min
Em-Rab7
DQ-BSA
F
DQ-BSA Em-Rab7
Late Endosome (DQ lo)
G
Mean Late Endosome Area (μm²)
LLOMe
DMSO
Time (sec)
H
Lysosome (DQ hi)
I
Mean Lysosome Area (μm²)

Figure 2 Rab7-positive late endosomes rapidly respond to LLOMe.
(A) Definitions of late endosomes versus lysosomes. Both late endosomes and lysosomes are positive for Rab7 (cyan) and lysosomal associated membrane protein 1 (LAMP1) (yellow) but can be distinguished based on degradative capacity. Late endosomes are degradatively low (CatB*lo* or DQ-BSA*lo,* magenta). Lysosomes are degradatively high (CatB*hi* or DQ-BSA*hi*, magenta). **(B)** NRK cells were immunostained for Rab7, LAMP1, and lysosomal hydrolase cathepsin B (CatB) following vehicle (DMSO) or 1mM LLOMe treatment for one hour (scale= 5µm, inset = 1µm) and imaged by Airyscan microscopy. Representative late endosomes (LEs, empty white arrowhead) and lysosomes (LYS, filled yellow arrowhead). Mander's correlation coefficients for CatB intensity on Rab7 space **(C)** and LAMP1 intensity on Rab7 space **(D)** were determined using Imaris and compared using student's t-test (n= 10 FOV per condition from 3 independent experiments, *$p<0.05$, Error bars indicate SD). **(E)** Live imaging of Emerald-Rab7^{WT} (EmRab7^{WT}) transfected NRK cells loaded with 5µg/mL of the degradative sensor DQ-BSA overnight (see *Video 2*) in the presence of 1mM LLOMe for 15 minutes. Still frames at the time points indicated are shown. Representative LEs (Rab7+DQ*lo*) and LYS (Rab7+DQ*hi*) are indicated by empty white arrowhead and filled yellow arrowhead, respectively. Close-up single channel still frames of a representative LE **(F)** and LYS **(H)** are shown as inverted contrast images. Average area of DQ*lo* LEs **(G)** and DQ*hi* LYS **(I)** per cell were quantified over time using Imaris (n= 10 (DMSO) and 9 (LLOMe) movies per condition). Individual examples of area changes over time are shown in Supplemental Figure 2 E.

Figure 3

A

DMSO

DMSO inset

Merge

Rab7/ALIX/CatB

CatB/ALIX

Rab7/ALIX

B

5min LLOMe

5min LLOMe inset

Merge

Rab7/ALIX/CatB

4.

2.

1.

3.

CatB/ALIX

Rab7/ALIX

C

Rab7

CatB

ALIX

1. Damaged LYS

2. Non-damaged LYS

3. Damaged LE

4. Non-damaged LE

D

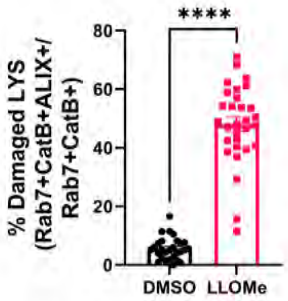

E

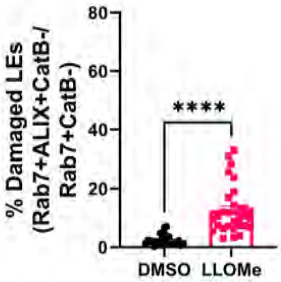

F

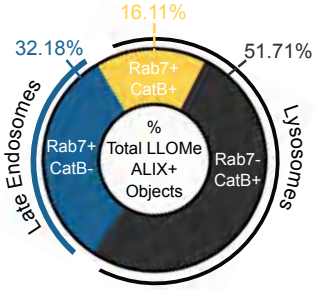

G

DMSO

DMSO inset

60min LLOMe

60min LLOMe inset

Rab7 Gal3

Rab7 Gal3

Figure 3 Most Rab7-positive late endosomes do not sustain membrane rupture after LLOMe

(A-C) Airyscan micrographs of primary MEFs immunostained for endogenous Rab7 (cyan), ALIX (yellow), and CatB (magenta) following vehicle (A) or 5-minute 1mM LLOMe treatment (B) (scale= 10µm, inset = 2µm). Representative examples for damaged LYS (1; CatB+ ALIX+), non-damaged LYS (2; CatB+ ALIX-), damaged LE (3; CatB- ALIX+), non-damaged LE (4; CatB- ALIX-) shown in **(C)**. **(D-E)** The percentage of total damaged LYS objects (C) and total damaged LE objects (D) were quantified using Imaris and compared using Welch's t- test (n= 30 FOV from 3 independent experiments, ****$p<0.0001$. Error bars indicate SEM.). **(F)** The proportion of ALIX+ objects in LLOMe that are LE vs LYS was determined using Imaris. **(G)** Airyscan micrographs of NRK cells treated with vehicle or 1mM LLOMe for 1 hour and immunostained for endogenous Rab7 and Gal3 (scale= 10µm, inset = 2µm). Rab7 intensity levels were artificially matched for viewing.

Figure 4

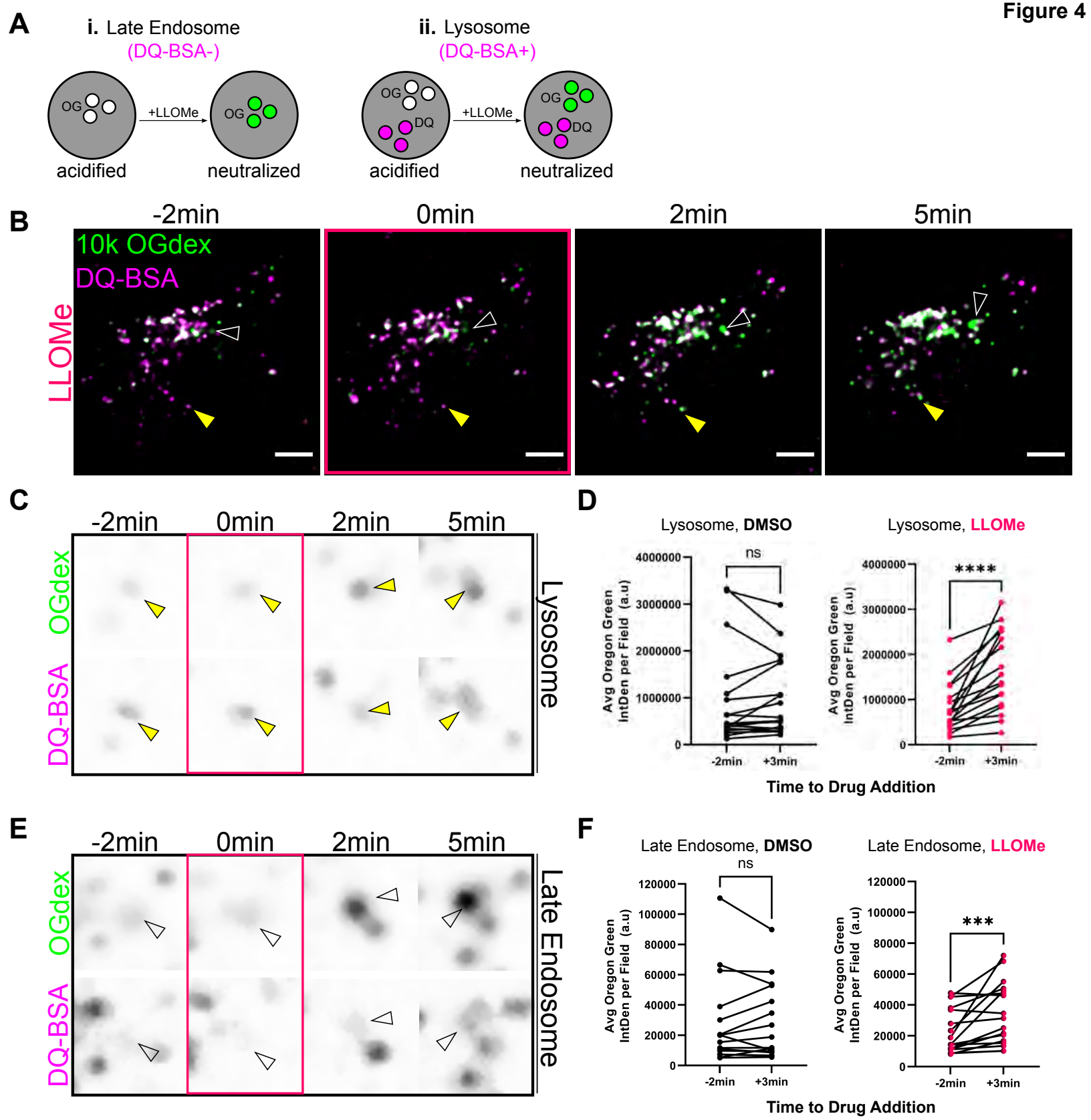
A
i. Late Endosome
(DQ-BSA-)
OG
+LLOMe
OG
acidified
neutralized
ii. Lysosome
(DQ-BSA+)
OG
DQ
+LLOMe
OG
DQ
acidified
neutralized
B
-2min
0min
2min
5min
10k OGdex
DQ-BSA
LLOMe
C
-2min
0min
2min
5min
OGdex
DQ-BSA
Lysosome
D
Lysosome, DMSO
Lysosome, LLOMe
ns
****
Avg Oregon Green IntDen per Field (a.u)
4000000
3000000
2000000
1000000
0
-2min
+3min
Time to Drug Addition
E
-2min
0min
2min
5min
OGdex
DQ-BSA
Late Endosome
F
Late Endosome, DMSO
Late Endosome, LLOMe
ns
***
Avg Oregon Green IntDen per Field (a.u)
120000
100000
80000
60000
40000
20000
0
-2min
+3min
Time to Drug Addition

Figure 4 LLOMe leads to pH collapse of Rab7 positive late endosomes and lysosomes.
(A) Schematic of pH dextran experiment: lysosomes were dually loaded with 100µg/mL pH sensitive 10 kDa FITC-dextran and pH-insensitive 10 kDa TMR-dextran. Lysosomal disruption with LLOMe de-quenches FITC fluorescence.
(B) Representative frames from spinning disk microscopy (see *Video 4*) of NRK cells preloaded with 5µg/mL degradative sensor DQ-BSA and acutely loaded with 100µg/mL pH-sensitive 10 kDa Oregon Green dextran (OGdex) for 1 hour, followed by 1mM LLOMe treatment and live imaging (G). Representative LEs (Rab7+DQ*lo*) and LYS (Rab7+DQ*hi*) are indicated by empty white arrowhead and filled yellow arrowhead, respectively. **(C)** Representative stills of de-quenching of OG fluorescence in a DQ*hi* LYS, indicative of pH neutralization. **(D)** OG fluorescence in DQ*hi* LYS was quantified at t=0 min and t= 3 min after DMSO (black dots) or 1 mM LLOMe (pink dots) using Imaris and compared using paired Wilcoxon Test. **(E)** Representative stills of de-quenching of OG fluorescence in a DQ*lo* LE, showing pH neutralization. **(F)** OG fluorescence in DQ*lo* LE was quantified at t=0 min and t= 3 min after DMSO (black dots) or 1 mM LLOMe (pink dots) using Imaris and compared using paired Wilcoxon Test (n= 15 movies per condition from 3 independent experiments, n.s. = non-significant, ***$p<0.001$).

Figure 5

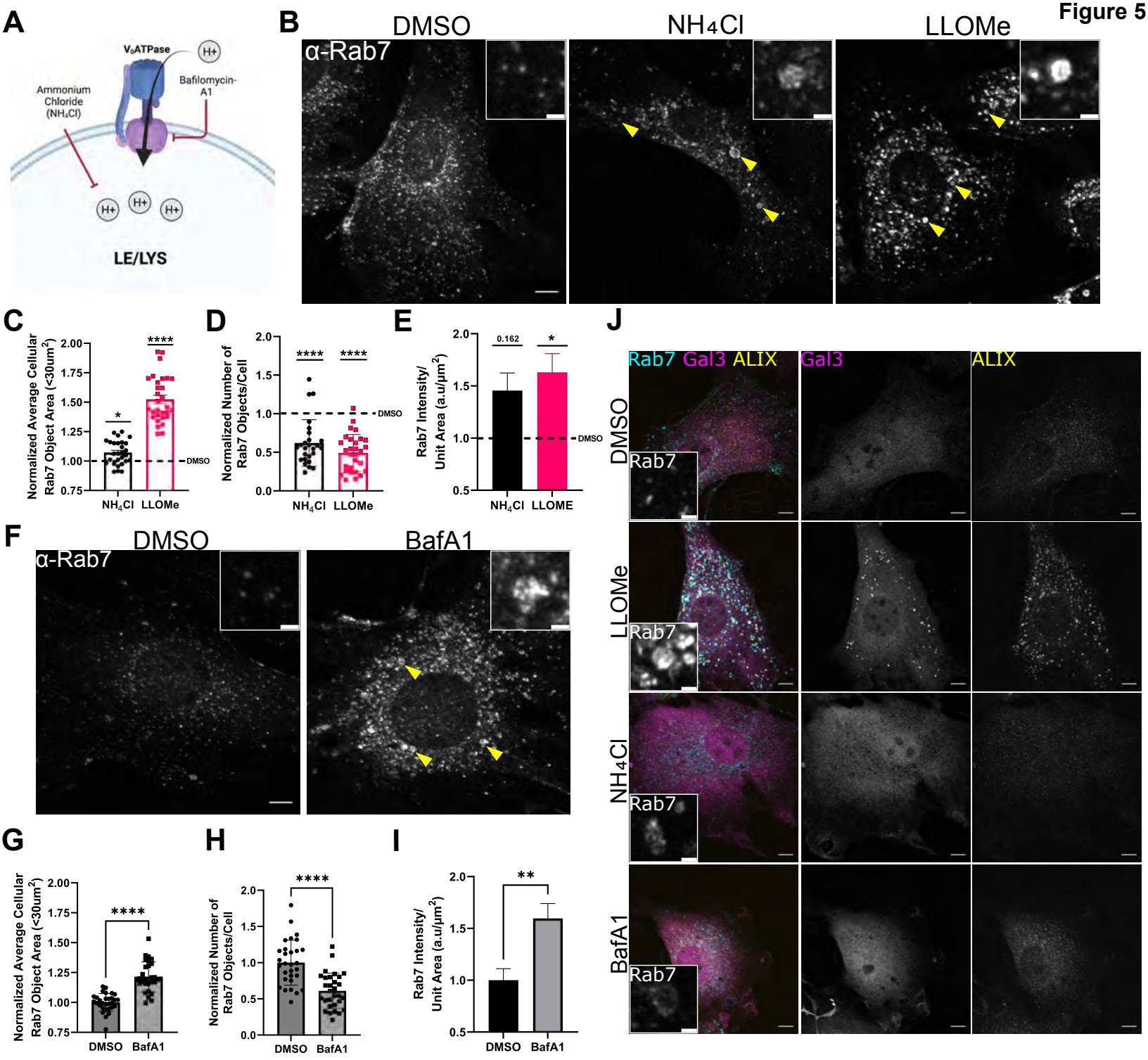
A
VₒATPase
H+
Ammonium Chloride (NH4Cl)
Bafilomycin-A1
LE/LYS
B
DMSO
NH4Cl
LLOMe
α-Rab7
C
Normalized Average Cellular Rab7 Object Area (<30um²)
NH4Cl
LLOMe
DMSO
D
Normalized Number of Rab7 Objects/Cell
E
Rab7 Intensity/ Unit Area (a.u/µm²)
0.162
F
BafA1
G
H
I
J
Rab7 Gal3 ALIX
Gal3
ALIX
Rab7
DMSO
LLOMe
NH4Cl
BafA1

Figure 5 pH gradient collapse is sufficient to phenocopy select LLOMe-driven Rab7 phenotypes

(A) Schematic for LE/LYS pH manipulation including acute use of the neutralizing base NH_4Cl and V_0-ATPase inhibitor Bafilomycin-A1 (BafA1).

(B-E) NH_4Cl induces Rab7 phenotypes reminiscent of LLOMe, but to a lesser degree. Widefield micrographs of primary mouse embryonic fibroblasts (MEFs) treated with vehicle (DMSO, 1 hour), NH_4Cl (20mM, 1 hour), and LLOMe (1mM, 1 hour) and immunostained for endogenous Rab7 (scale = 10µm, inset= 2µm) (B). Using Imaris, Rab7 surfaces were created and filtered for those <30µm^2 in area. Cumulative cellular surface properties were analyzed for average area of Rab7 surfaces per cell (C), number of Rab7 surfaces per cell (D), and Rab7 intensity per unit area of created surfaces (E). Number, area, and intensity measurements were compared using Ordinary One-Way ANOVA, Welch's ANOVA, and Kruskal Wallis tests, respectively (n= 30 FOV from 3 independent experiments, n.s. = not significant, *p<0.05, **p<0.01, ***p<0.001, ****p<0.0001. Error bars indicate SEM.). **(F-I) BAF-A1 partially phenocopies Rab7 phenotypes of LLOMe**. Widefield micrographs of primary MEFs treated with vehicle (DMSO, 1hr) and BafA1 (200nM for 2 hours) and immunostained for endogenous Rab7 (scale = 10µm, inset= 2µm) (F). (G-I) Quantification and comparisons were performed in parallel to and exactly as described in (C-E).

(J) Membrane rupture is only observed in LLOMe but not NH_4Cl or BAF-A1. Widefield micrographs of primary MEFs treated with vehicle (DMSO, 1 hour), LLOMe (1mM, 1 hour), NH_4Cl (20mM, 1 hour), and BafA1 (200nM, 2 hour) and immunostained for endogenous Rab7, ALIX, and Gal3 (scale = 10µm, inset= 2µm).

Figure 6

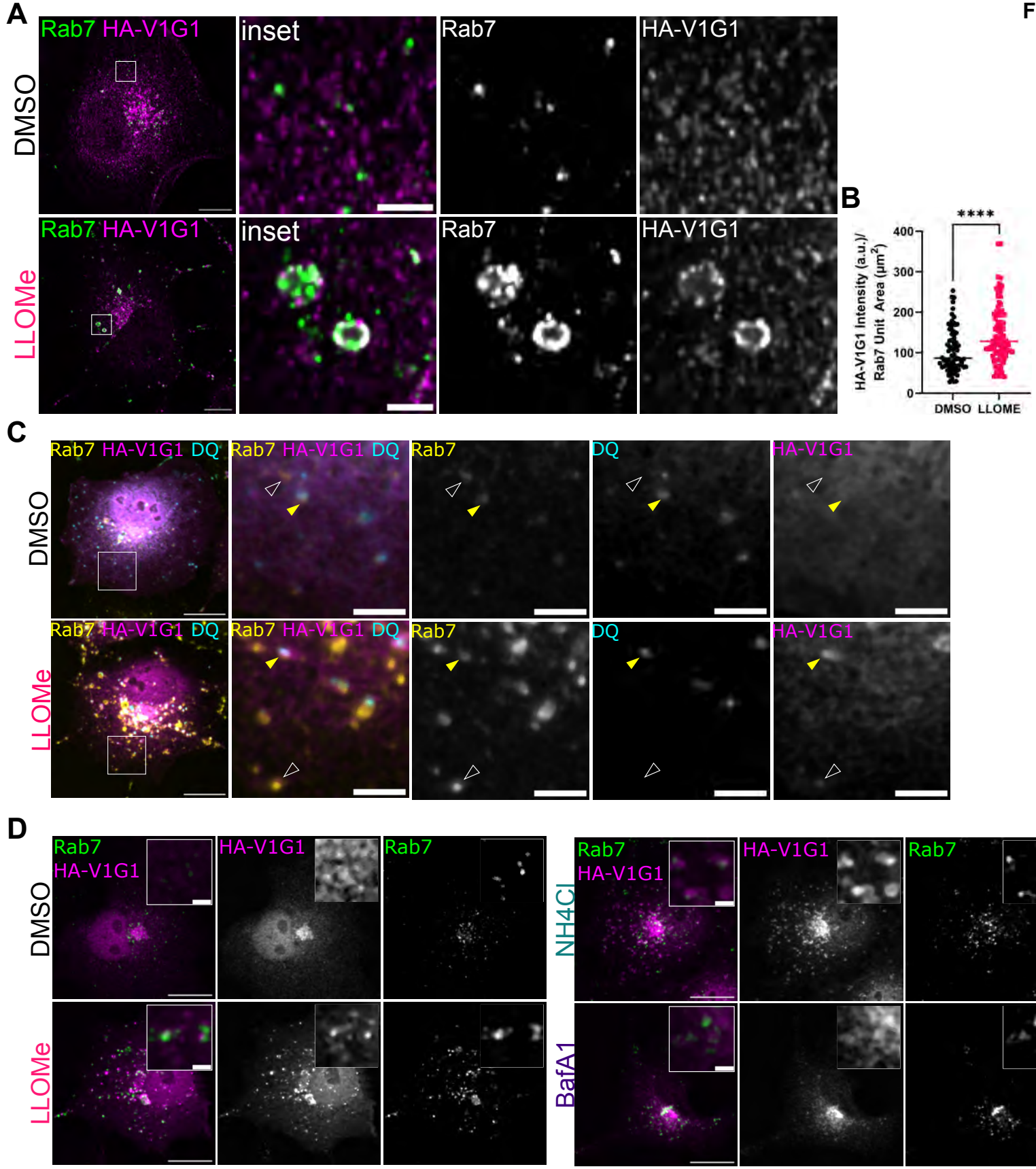
A
Rab7 HA-V1G1
inset
Rab7
HA-V1G1
DMSO
LLOMe
B
****
HA-V1G1 Intensity (a.u.)/ Rab7 Unit Area (μm²)
400
300
200
100
0
DMSO
LLOME
C
Rab7 HA-V1G1 DQ
Rab7
DQ
HA-V1G1
D
NH4Cl
BafA1
E
p>0.9999
****
***
p>0.9999
Number of HA-V1G1 Compartments per Cell
DMSO
LLOMe
NH4Cl
BafA1
F
p=0.0764
Average Cellular HA-V1G1 Compartment Area (μm²)
2.0
1.5
1.0
0.5
0.0

Figure 6 LLOMe-mediated pH collapse recruits the V_1G_1 subunit of the V-ATPase to late endosomes and lysosomes

(A, B) V_1G_1 is recruited to enlarged Rab7 endosomes after LLOMe. Confocal micrographs of COS-7 cells transfected with HA-V_1G_1 and treated with either vehicle or 1mM LLOMe for 30 minutes, then immunostained for endogenous Rab7 and the HA-epitope tag (scale= 10µm, inset = 2µm) (A). Quantification of (A) is shown in (B) demonstrating the intensity of V_1G_1 per masked Rab7 unit area per cell compared using Mann Whitney U test (n= 76 (DMSO) and 85 (LLOMe) equivalently transfected cells from 3 independent experiments, ****$p<0.0001$).

(C) V_1G_1 is recruited to both DQ*lo* and DQ*hi* compartments in LLOMe. Widefield micrographs of HA-V_1G_1 transfected COS-7 cells. Cells were loaded with 5µg/mL DQ-BSA overnight and treated with vehicle (DMSO) or 1mM LLOMe for 30 minutes, fixed, and immunostained for endogenous Rab7 and HA, demonstrating (scale= 20µm, inset= 5µm). Representative LEs (Rab7+DQ*lo*) and LYS (Rab7+DQ*hi*) are indicated by empty white arrowhead and filled yellow arrowhead, respectively.

(D-F) NH_4Cl but not BAF-A1 recruits V_1G_1. Widefield micrographs of COS-7 cells transfected with HA-V_1G_1 and treated with vehicle (DMSO, 1 hour), NH_4Cl (20mM, 1 hour), LLOMe (1mM, 1 hour), and BafA1 (200nM, 2 hours) and immunostained for endogenous Rab7 and the HA-epitope tag (D) (scale= 20µm inset= 2µm). The number (E) and area (F) of peripheral HA-V_1G_1 compartments were quantified for each condition and compared using Kruskal-Wallis test [n= 47 (DMSO), 63 (LLOMe), 56 (NH_4Cl), 51 (BafA1) HA-V_1G_1 equivalently transfected cells from 3 independent experiments, n.s. = not significant, *$p<0.05$, **$p<0.01$, ***$p<0.001$, ****$p<0.0001$].

Figure 7

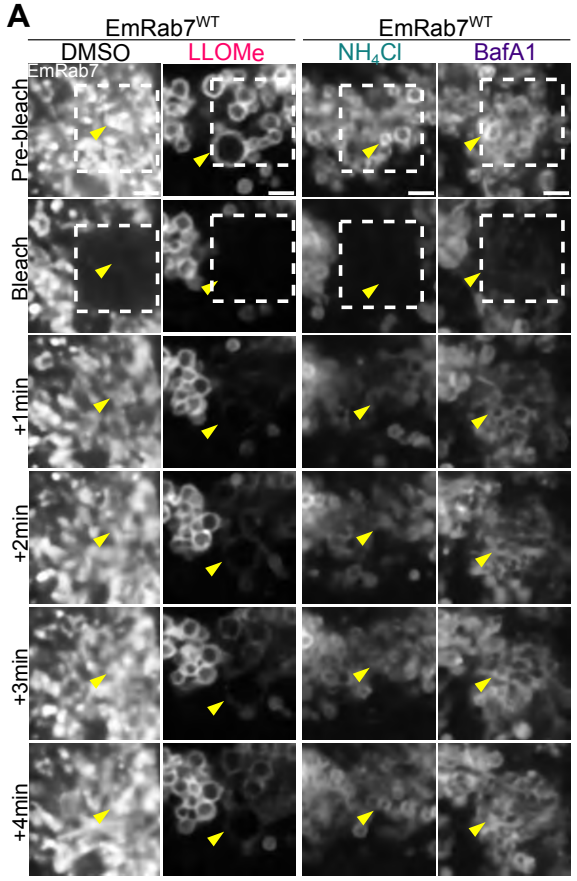

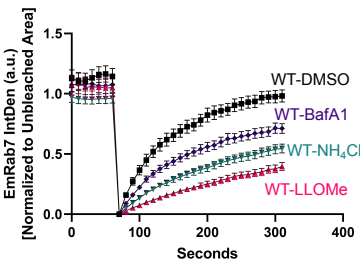

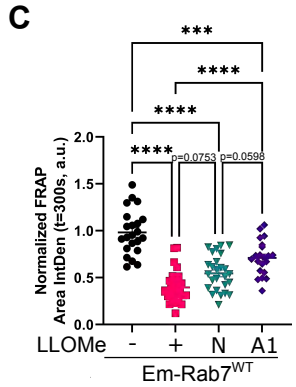

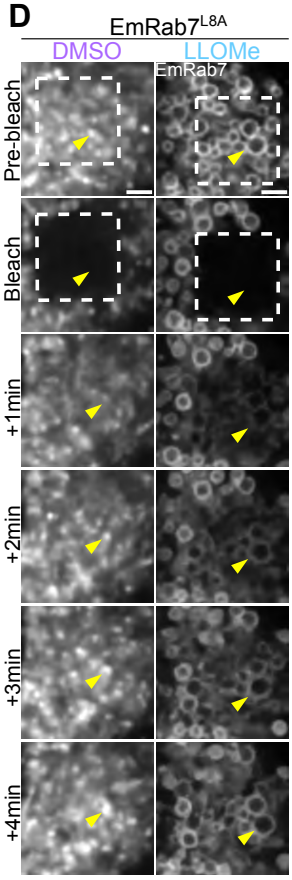

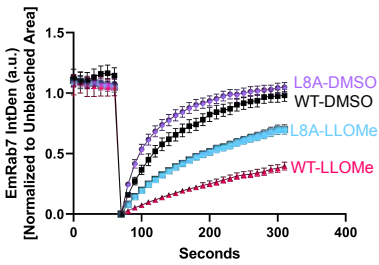

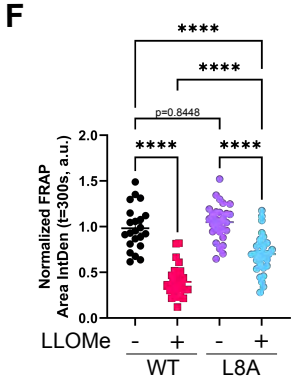

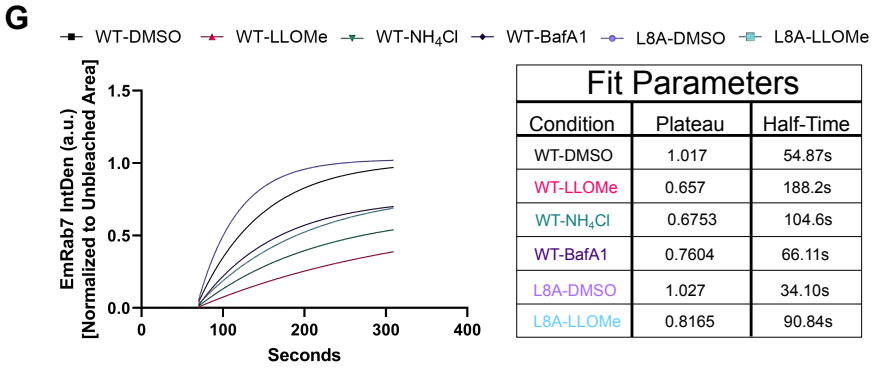

Fit Parameters

Condition	Plateau	Half-Time
WT-DMSO	1.017	54.87s
WT-LLOMe	0.657	188.2s
WT-NH_4Cl	0.6753	104.6s
WT-BafA1	0.7604	66.11s
L8A-DMSO	1.027	34.10s
L8A-LLOMe	0.8165	90.84s

H

FRAP Summary

Condition	V-ATPase Assembly	RILP binding	Rab7 stabilization
WT-DMSO	LOW	Present	----
WT-LLOMe	HIGH	Present	↑↑↑
WT-NH_4Cl	HIGH	Present	↑↑↑
WT-BafA1	LOW	Present	↑
L8A-DMSO	LOW	Absent	—
L8A-LLOMe	HIGH	Absent	↑

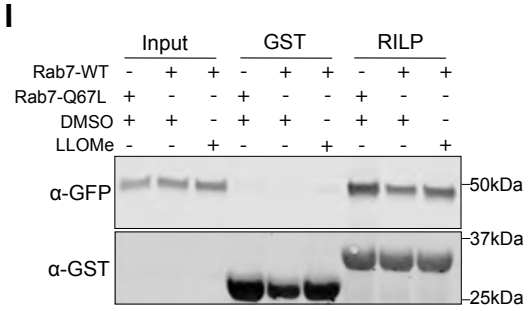

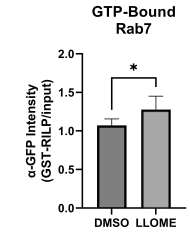

Figure 7 LLOMe drives membrane stabilization and hyperactivation of Rab7 through influence from V-ATPase assembly and RILP

(A-C) Stability of Rab7 on endosomes is influenced by V-ATPase assembly (A) Representative stills from confocal fluorescence recovery after photobleaching (FRAP) live imaging (see *Video 5*) of EmRab7^{WT} expressing cells under vehicle (DMSO, 10mins, n=23), LLOMe (1mM, 10mins, n=27), NH_4Cl (20mM, 10mins, n=26), or BafA1 (200nM, 1 hour, n=21) conditions. Bleached area indicated by dashed white box (33.0625μm^2 area) with representative Rab7+ endosomes indicated by solid yellow arrowhead. (scale = 2μm). (B) FRAP recovery curves were scaled to the minimum intensity value at time of bleaching, and normalized to an equivalent unbleached area for each condition, then plotted over time, for DMSO and pH neutralizing conditions. (C) Mean FRAP area intensity values were determined at t= 300 sec (Y_{max}) and compared using Ordinary One-Way ANOVA (n= as listed in (A) from 3 independent experiments, n.s. = not significant, *p<0.05, ****p<0.0001). **(D-F) Stability of Rab7 on endosomes is influenced by RILP in response to pH neutralization**. (D) Representative stills from confocal fluorescence recovery after photobleaching (FRAP) live imaging (see *Video 5*) of mutant EmRab7^{L8A} expressing cells under vehicle (DMSO, 10mins, n=28) or LLOMe (1mM, 10mins, n=30). Bleached area indicated by dashed white box (33.0625μm^2 area) with representative Rab7+ endosomes indicated by solid yellow arrowhead. (scale = 2μm). (E) FRAP recovery curves were scaled to the minimum intensity value at time of bleaching, and normalized to an equivalent unbleached area for each condition, then plotted over time, for wild-type and mutant conditions. (F) Mean FRAP area intensity values were determined at t= 300 sec (Y_{max}) and compared using Ordinary One-Way ANOVA (n= as listed in (A) from 3 independent experiments, n.s. = not significant, *p<0.05, ****p<0.0001). Wild-type data in (D-E) are identical to that of (A-C); mutant data has been separated for clarity.

(G) ***Left:*** One-way exponential phase association fitted curves for all conditions following bleach. ***Right:*** Fitted parameters from one-way exponential phase association curves indicating the fitted plateau values and half-time ($t_{1/2}$) values for each condition. **(H)** Summary table for all conditions based on degree of V-ATPase assembly and RILP binding, with subsequent effects on Rab7 membrane stability. **(J-I)** Representative immunoblot of GST- or GST-RILP immunocaptured lysates from GFP-Rab7 transfected COS-7 cells treated with either DMSO or 1mM LLOMe (1 hour), to probe for GTP-bound Rab7 (H). Rab7^{Q67L} was used as a positive control to determine top range of cellular GTP-Rab7 binding achievable in COS-7 cells. RILP-bound GFP-Rab7 in DMSO and LLOMe treated conditions were quantified from densitometry analyses of Western blots (I) using student's t-test in (n= 5 independent experiments, *p<0.05. Error bars indicate SEM.)

Figure 8

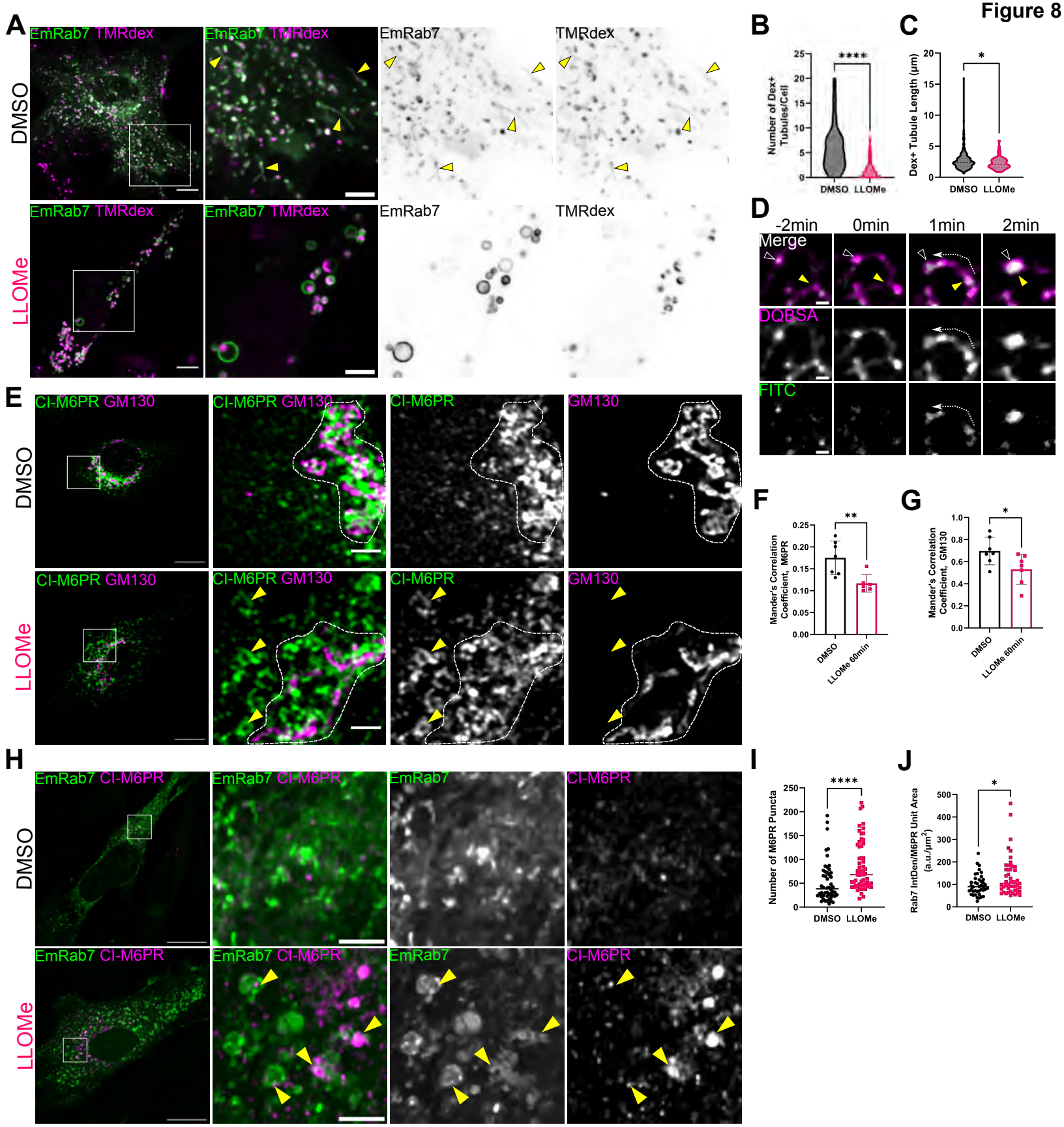
A
EmRab7 TMRdex
EmRab7
TMRdex
DMSO
LLOMe
B
Number of Dex+ Tubules/Cell
****
DMSO
LLOMe
C
Dex+ Tubule Length (µm)
*
D
-2min
0min
1min
2min
Merge
DQBSA
FITC
E
CI-M6PR GM130
CI-M6PR
GM130
F
Mander's Correlation Coefficient, M6PR
**
LLOMe 60min
G
Mander's Correlation Coefficient, GM130
H
EmRab7 CI-M6PR
I
Number of M6PR Puncta
J
Rab7 IntDen/M6PR Unit Area (a.u./µm²)

Figure 8 Hyperactivation of Rab7 leads to deficits in Rab7 compartment tubulation and receptor trafficking

(A-D) LLOMe leads to deficits in Rab7+ compartment tubulation. (A) Confocal micrographs of Em-Rab7^{WT} transfected primary MEFs. MEFs were loaded with 100µg/mL tetramethyl-rhodamine (TMR; red) dextran for 2 hours and chased for 2 hours, prior to treatment with either vehicle (DMSO) or 1mM LLOMe for 45 minutes. Em-Rab7^{WT} tubules (green) are indicated with solid yellow arrowheads (scale= 10µm, inset= 5µm). **(B)** Quantification of the number of dextran containing Em-Rab7^{WT} tubules in (A), compared using Mann-Whitney U test (n= 57 (DMSO) and 50 (LLOMe) transfected cells from 3 independent experiments, ****p<0.0001). **(C)** Quantification of the length of dextran containing Em-Rab7^{WT} tubules from conditions in (A), compared using Mann Whitney U test (n= 331 tubules from 57 cells (DMSO) and 64 tubules from 50 cells (LLOMe) from 3 independent experiments, *p<0.05). **(D)** Representative stills from live imaging (see *Video 6*) of LLOMe treated MEFs loaded with 5µg/mL DQ-BSA overnight and 100µg/mL fluorescein (FITC) dextran for 30 minutes prior to imaging. Filled yellow arrowhead indicates the terminal end of a tubule collapsing into its source endosome (unfilled white arrowhead).

(E-J) LLOMe leads to mistargeting of CI-M6PR. NRK cells were immunostained for endogenous CI-M6PR (green) and GM130 (magenta) following DMSO (top row) or 1mM LLOMe (bottom row) treatment (scale= 5µm, inset = 1µm), and imaged with Airyscan microscopy (E). Single channels are shown in black and white. The GM130-positive Golgi area is outlined in white. Peripherally mis-localized CI-M6PR is indicated by filled yellow arrowheads. Mander's correlation coefficients for CI-M6PR intensity on GM130 space (F) and GM130 intensity on CI-M6PR space (G) were determined using Imaris and compared using student's t-test (n= 10 FOV per condition from 3 independent experiments, *p<0.05, Error bars indicate SD). **(H)** Confocal micrographs of primary MEFs transfected with EmRab7 and treated with either DMSO or LLOMe for 1 hour were fixed and stained for endogenous CI-M6PR (scale= 20µm, inset = 3µm). **(I)** Quantification of the total number of CI-M6PR puncta in (H). **(J)** Quantification of the intensity of Em-Rab7^{WT} signal on masked CI-M6PR area in (H). For I-J, conditions were compared using Mann-Whitney U test (n= 40 transfected cells per condition from 3 independent experiments, *p<0.05, ****p<0.0001).

Figure 9

A

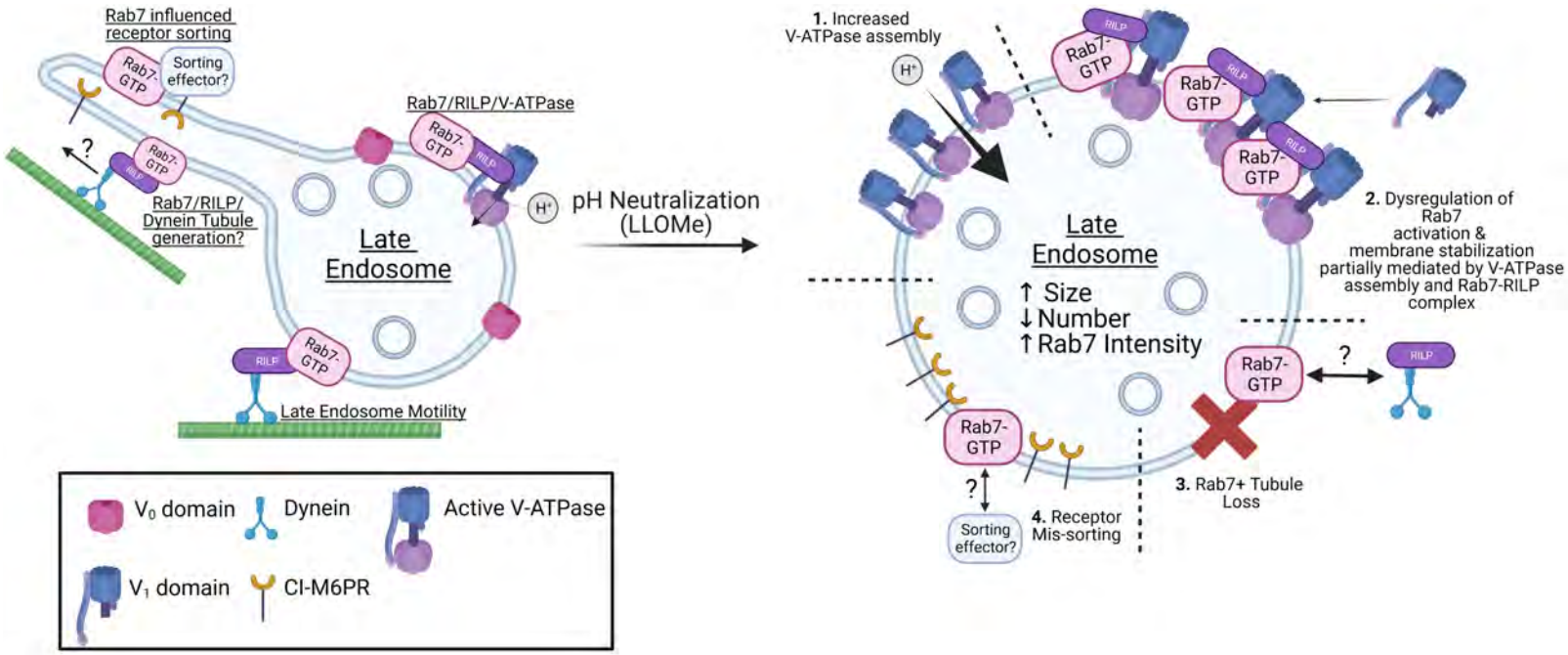
Rab7 influenced receptor sorting
Rab7-GTP
Sorting effector?
Rab7/RILP/V-ATPase
Rab7-GTP
RILP
?
Rab7-GTP
RILP
Rab7/RILP/ Dynein Tubule generation?
Late Endosome
H+
pH Neutralization (LLOMe)
RILP
Rab7-GTP
Late Endosome Motility
V0 domain
Dynein
Active V-ATPase
V1 domain
CI-M6PR
1. Increased V-ATPase assembly
H+
Rab7-GTP
RILP
Late Endosome
↑ Size
↓ Number
↑ Rab7 Intensity
2. Dysregulation of Rab7 activation & membrane stabilization partially mediated by V-ATPase assembly and Rab7-RILP complex
Rab7-GTP
?
RILP
3. Rab7+ Tubule Loss
Rab7-GTP
?
Sorting effector?
4. Receptor Mis-sorting

Figure 9 The current model for behavior of undamaged Rab7-positive late endosomes in response to LLOMe mediated pH neutralization

(A) pH neutralization of late endosomes via LLOMe treatments initiates alterations to both V-ATPase and Rab7 behavior. *Left:* Normal Rab7-effector behaviors on late endosomes that contribute to late endosome function. Rab7-RILP complexes interact with dynein motors and microtubules to contribute to late endosomal motility and tubule generation. Rab7 interacts with receptor sorting machineries (e.g., retromer). Proper receptor recycling ensures CI-M6PR levels are low in late endosomes and absent from lysosomes. Rab7 also is in complex with RILP and the V-ATPase subunit V_1G_1. There is baseline acidification of late endosomes through assembled V-ATPase complexes, and membrane embedded V_0 that are not in complex with V_1 domains. *Right:* Following LLOMe mediated pH neutralization, V_1G_1 is increasingly recruited to endosomes indicative of V-ATPase assembly. As a partial consequence of V-ATPase assembly, Rab7 is stabilized on the membrane and hyper activated. RILP binding further stabilizes Rab7. As a consequence of Rab7 hyper-stabilization, other effector functions (i.e., tubulation and receptor sorting) are lost.